

As a library, NLM provides access to scientific literature. Inclusion in an NLM database does not imply endorsement of, or agreement with, the contents by NLM or the National Institutes of Health.

Learn more: [PMC Disclaimer](#) | [PMC Copyright Notice](#)



J Neurophysiol. 2017 Feb 22;117(6):2163–2178. doi: [10.1152/jn.00240.2016](https://doi.org/10.1152/jn.00240.2016)

Spaceflight-induced synaptic modifications within hair cells of the mammalian utricle

David R Sultemeier¹, Kristel R Choy¹, Felix E Schweizer^{2,3}, Larry F Hoffman^{1,3,✉}

[Author information](#) [Article notes](#) [Copyright and License information](#)

PMCID: PMC5454470 PMID: [28228581](https://pubmed.ncbi.nlm.nih.gov/28228581/)

Spaceflight imposes a radically different sensory environment from that in which the inner ear utricle normally operates. We investigated synaptic modifications in utricles from mice flown aboard a space shuttle mission. Structural synaptic plasticity was detected in the medial extrastriola, a region associated with encoding static head position, as decreased synapse density. These results are remarkably congruent with a recent report of decreased utricular function in astronauts immediately after returning from the International Space Station.

Keywords: synaptic ribbon, ribeye, CtBP2, Shank1a, plasticity, resampling, linear mixed effects

Abstract

Exposure to the microgravity conditions of spaceflight alleviates the load normally imposed by the Earth's gravitational field on the inner ear utricular epithelia. Previous ultrastructural investigations have shown that spaceflight induces an increase in synapse density within hair cells of the rat utricle. However, the utricle exhibits broad physiological heterogeneity across different epithelial regions, and it is unknown whether capabilities for synaptic plasticity generalize to hair cells across its topography. To achieve systematic and broader sampling of the epithelium than was previously

conducted, we used immunohistochemistry and volumetric image analyses to quantify synapse distributions across representative utricular regions in specimens from mice exposed to spaceflight (a 15-day mission of the space shuttle Discovery). These measures were compared with similarly sampled Earth-bound controls. Following paraformaldehyde fixation and microdissection, immunohistochemistry was performed on intact specimens to label presynaptic ribbons (anti-CtBP2) and postsynaptic receptor complexes (anti-Shank1A). Synapses were identified as closely apposed pre- and postsynaptic puncta. Epithelia from horizontal semicircular canal cristae served as “within-specimen” controls, whereas utricles and cristae from Earth-bound cohorts served as experimental controls. We found that synapse densities decreased in the medial extrastriolae of microgravity specimens compared with experimental controls, whereas they were unchanged in the striolae and horizontal cristae from the two conditions. These data demonstrate that structural plasticity was topographically localized to the utricular region that encodes very low frequency and static changes in linear acceleration, and illuminates the remarkable capabilities of utricular hair cells for synaptic plasticity in adapting to novel gravitational environments.

NEW & NOTEWORTHY Spaceflight imposes a radically different sensory environment from that in which the inner ear utricle normally operates. We investigated synaptic modifications in utricles from mice flown aboard a space shuttle mission. Structural synaptic plasticity was detected in the medial extrastriola, a region associated with encoding static head position, as decreased synapse density. These results are remarkably congruent with a recent report of decreased utricular function in astronauts immediately after returning from the International Space Station.

SENSORY ADAPTATION may be manifested as an alteration in the coding of natural stimuli subsequent to changes in the ambient sensory environment. For inner ear gravity receptors, the utricle and saccule, this environment is dominated by Earth gravity, which is constant over an organism’s lifetime, and chronic alterations in receptor loading are not known to exist. However, alterations in the gravity environment are experienced with spaceflight, and they can be implemented in the laboratory through chronic centrifugation. This raises questions concerning the capabilities of these sensory epithelia for adaptive modifications that may result from exposure to ambient gravitational field alterations, despite the absence of natural conditions in which such alterations may exist.

Previous spaceflight studies have demonstrated that hair cells of the mammalian utricle exhibit the capability for synaptic plasticity ([Ross 1993, 1994, 2000](#); [Ross and Varelas 2005](#)). In these studies, which were based on analyses of serial transmission electron micrographs, it was reported that microgravity exposures of 9–13 days resulted in synaptic ribbon density increases within utricular hair cells. The greatest changes were found in specimens harvested in-flight (i.e., avoiding the gravity transitions associated with return to Earth gravity). Although increased synapse densities were found in both type I and II hair cells in flight-harvested specimens, analyses were not conducted from multiple loci across the topography of the utricle, and therefore it is not known whether parallel changes occurred in hair cells from different utricular regions. This is particularly important in view of the heterogeneity of response characteristics reflected by afferents projecting from different utricular regions ([Goldberg et al. 1990a, 1990b](#)).

The significance of Ross's findings is the demonstration that adult utricular hair cells can undergo synaptic modifications, despite the absence of any obvious conditions in which they would be naturally invoked. As noted above, it has yet to be determined whether hair cells in all regions of the utricle exhibit the capacity for synaptic plasticity. Resolution of this question will be informative of the underlying factors driving the synaptic modifications in view of the differential sensitivity to dynamic linear acceleration stimuli across the utricular topography. For example, afferents projecting from extrastriolar and striolar utricular regions exhibit heterogeneity in their dynamic response characteristics ([Eatock and Songer 2011](#)), whereby the low-pass characteristics of extrastriolar afferents enable them to signal steady-state changes in head orientation relative to Earth gravity ([Fernández and Goldberg 1976a; Goldberg et al. 1990b](#)). In contrast, steady-state stimuli are less effectively transmitted by striolar afferents ([Fernández and Goldberg 1976a; Goldberg et al. 1990a, 1990b](#)) due to pre- and postsynaptic factors that include the expression of delayed rectifier potassium conductances in type I hair cells ([Rüschen et al. 1998](#)) and low-voltage-activated potassium conductances in afferent calyces ([Lysakowski et al. 2011; Meredith and Rennie 2015](#)). Consequently, a finding of structural plasticity confined to the extrastriola would be consistent with the preferential sensitivity to steady-state stimuli within this region and a reflection of potential afferent response modifications in the new gravitational environment. On the other hand, plasticity found in all regions of the utricle could also result from a variety of uncontrolled variables associated with the spaceflight environment that are not specifically related to gravity (e.g., radiation).

In this report, we present our findings of synapse quantification from the utricles of mice that constituted a portion of the biological payload aboard the space shuttle Discovery on STS-131, which launched on April 5, 2010, and landed on April 20, 2010. We analyzed these specimens for structural synaptic plasticity by using immunohistochemical methods to identify closely apposed immunofluorescent puncta representing presynaptic ribbons and postsynaptic receptor complexes. These specimens were compared with those harvested from control mice that were maintained in habitat modules identical to those housing animals on the shuttle middeck, and for identical periods. Our goal was to produce a broad perspective of the utricle's capabilities for synaptic plasticity through a topography-based sampling strategy.

METHODS

This study was conducted as part of the Biospecimen Sharing Program (BSP) organized and managed by the National Aeronautics and Space Administration (NASA). The program comprised eight individual experiments with scientific objectives that ranged from biochemical and ultrastructural analyses of salivary glands to vasomotor experiments evaluating vascular dynamics in major arteries supplying load-bearing muscles ([Bailey et al. 2014; Behnke et al. 2013; Blaber et al. 2013; Mednieks et al. 2014; Stabley et al. 2012](#)). Therefore, it is important to note that the conditions of specimen harvest and processing were constrained to those that optimized a broad range of mission scientific objectives. This impacted the present study in the progress of specimens through the harvesting procedures and the selection of a postsynaptic marker, which will be discussed below.

Animals and Microgravity Exposure

Flight (referred to hereafter as “microgravity”) and control animals were 16-wk-old (at time of landing) female C57Bl/6J mice (Jackson Laboratories). For this study we report on inner ear specimens obtained from four animals of each group. Both microgravity and control groups were maintained in NASA Animal Enclosure Modules (AEMs) for identical periods of time based on the duration of the spaceflight mission. The AEMs were self-contained environmental housing quarters providing ad libitum food and water, sufficient air exchange, temperature and humidity control, and a 12:12-h light-dark cycle. All procedures that affected these animals were approved by the Institutional Animal Care and Use Committee of the NASA/Ames Research Center (Moffett Field, CA).

The total mission duration was 15 days 2.8 h, during which time the AEMs remained on the Discovery orbiter middeck. This included the periods of gravity transition at launch (1G to microgravity) and landing (microgravity to 1G), during which time the gravitational exposures are intense and variable. In the present study, animals were exposed to both transition periods in addition to the ~2 wk of microgravity. The AEMs were delivered to the Space Life Sciences Laboratory at Kennedy Space Center ~2 h after landing, at which time the animals underwent a health examination. The first animal was anesthetized ~3 h after landing. Flight animals serially entered the processing queue on ~15-min intervals. The entire cohort of microgravity animals was processed before the control group.

Our early efforts to validate the use of pre- and post-synaptic markers included the use of utricle specimens from the Y16 transgenic mouse line, in which yellow fluorescent protein (YFP) expression is driven by the *thy-1* promoter ([Feng et al. 2000](#)). In these animals, neuronal subsets, including many vestibular afferent neurons, exhibit YFP fluorescence that proved advantageous in evaluating synaptic markers. YFP-positive specimens were processed in precisely the same fashion as all others in this investigation.

Specimen Harvesting

The BSP activities followed those of the primary investigation for this mission involving studies of immune responses to an in-flight challenge ([Chang et al. 2015](#)). Only non-immunochallenged control animals were used for the BSP investigations. Animals were euthanized immediately after final handling by the immunology investigation team. The time between euthanasia and delivery to the BSP dissection teams was 5.7 min (± 1.1 min) for the microgravity group and 4.8 min (± 0.5 min) for the control group. The intact central nervous system was first removed for another BSP investigator team, which required an additional 1 min. The temporal bones were then rapidly excised; one labyrinth from each of four animals was utilized for the present study, and fixative (4% paraformaldehyde in 0.1 M Sorensen’s phosphate buffer, pH 7.4) was infused into the vestibule through a fenestra made in the temporal bone dorsal to the posterior semicircular canal nerve. The floor of the subarcuate fossa was then debrided to visualize the entire utricle, and the membranous labyrinth was opened to allow the utricle and otolithic membrane to be exposed to fixative. The otolithic membrane was removed by a gentle stream of fixative, and the entire temporal bone was placed in fixative for 3 h. After this period of immersion fixation, each temporal bone was thoroughly rinsed with phosphate-buffered saline (PBS) and stored in a solution of 10% sucrose in PBS for shipment to our University of California, Los Angeles

(UCLA) laboratories.

Immunohistochemical Processing

Vestibular epithelia from flight and control temporal bones were dissected and processed intact for immunohistochemical identification of afferent synapses within hair cells and the complementary postsynaptic complex. Information regarding the primary antibodies and the controls used to verify their efficacy is included in [Table 1](#). The protein ribeye is the major structural component of synaptic ribbons ([Schmitz et al. 2000](#)) and is made from a splice variant of the gene coding for the transcription factor COOH-terminal binding protein 2 (CtBP2). Antibodies to CtBP2 were thus used to label synaptic ribbons within utricular hair cells ([Braude et al. 2015](#); [Dulon et al. 2009](#); [Sadeghi et al. 2014](#)). Shank1a is a postsynaptic density protein that has been identified in glutamatergic receptor scaffolds, and anti-Shank1a antibodies have been used as a postsynaptic marker in a variety of tissues, including utricle and cochlea ([Braude et al. 2015](#); [Huang et al. 2012](#)) as well as retina ([Stella et al. 2012](#)). In the mouse utricle, Shank1a colocalized with virtually all PSD95 immunolabeled puncta, whereas no evidence of Shank2 or Shank3 expression was found ([Braude et al. 2015](#)). At the time our processing was conducted, direct labeling of AMPA receptor subunits was considerably less reliable, requiring very short fixation times that could not be accommodated in view of the timing constraints imposed by the postflight processing workflow. Therefore, we used anti-Shank1a as a postsynaptic marker because it proved very reliable with standard fixation times that were readily managed in the specimen harvest queue.

Table 1.

Antibody inventory for synapse identification in microgravity and control utricles

Target	Manufacturer (Product no.); Purification	Immunogen	Host (Mono- or Polyclonal)	Working Concentration	Positive Control	Negative Control
CtBP2	BD Biosciences (612044); affinity purified	Amino acids 361–445 of mouse CtBP2	Mouse (monoclonal)	1:250	Braude et al. (2015)	Primary Ab omission
Shank1a	Neuromics (19016); affinity purified	Peptide mapping COOH-terminus of rat Shank1a	Rabbit (polyclonal)	1:250	Braude et al. (2015)	Stella et al. (2012) ; Primary Ab omission

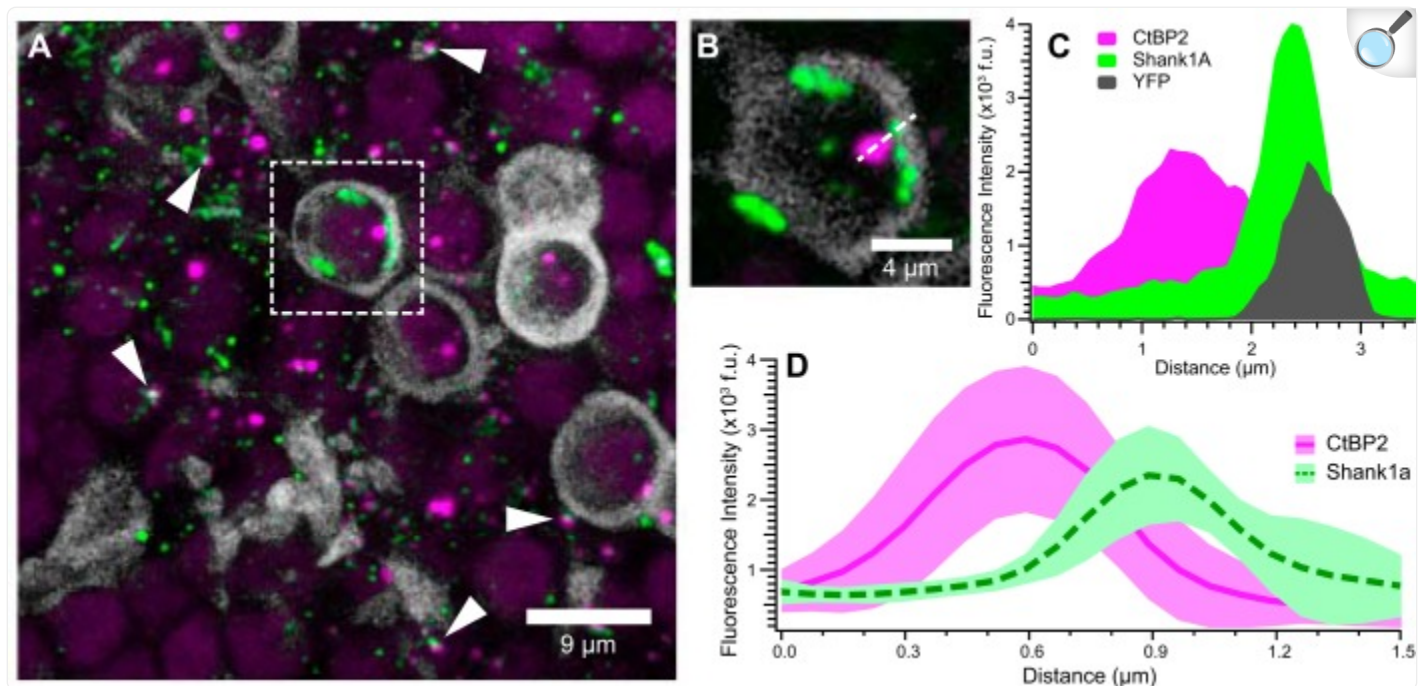
[Open in a new tab](#)

Immunohistochemical processing proceeded as follows. Intact vestibular epithelia were incubated in blocking solution (0.25% Triton X-100, 1.0% BSA solution in PBS) for 2 h at room temperature and then incubated 48–72 h at 4°C in a primary antibody cocktail that included anti-CtBP2 (1:250; mouse anti-CtBP2) and anti-Shank1a (1:250; rabbit anti-Shank1a) in blocking solution. At the conclusion of the incubation period in primary antibodies, specimens were washed in 0.1 M PBS (3 times for 10 min). The tissues were then incubated at room temperature in a cocktail of secondary antibodies and stains diluted in blocking solution that included Alexa Fluor 546-conjugated goat anti-mouse IgG antibody (1:500; A-11030; Thermo Fisher Scientific, Waltham, MA), Alexa Fluor 488-conjugated goat anti-rabbit IgG antibody (1:500; A-11034; Thermo Fisher Scientific), and Alexa Fluor 633-conjugated phalloidin (1:500; A-22284; Thermo Fisher Scientific). Tissue was mounted on glass slides with one to two spacers (S-24735; Thermo Fisher Scientific) in Vectashield HardSet mounting medium with 4',6-diamidino-2-phenylindole (DAPI; H-1500; Vector Laboratories, Burlingame, CA).

A minimal modification was made to accommodate the intrinsic expression of YFP in afferent neuron calyces in studies to validate the use of anti-Shank1a as a postsynaptic marker. For these specimens we used different secondary antibodies to change the Shank1a immunolabeling to the 546-nm excitation line and the CtBP2 immunolabeling to the 633-nm excitation line. The colors depicted in [Fig. 3](#) were selected to maintain consistency with respect to CtBP2 and

Shank1a, despite the alterations in actual emission characteristics of the secondary antibodies in these specimens.

Fig. 3.



[Open in a new tab](#)

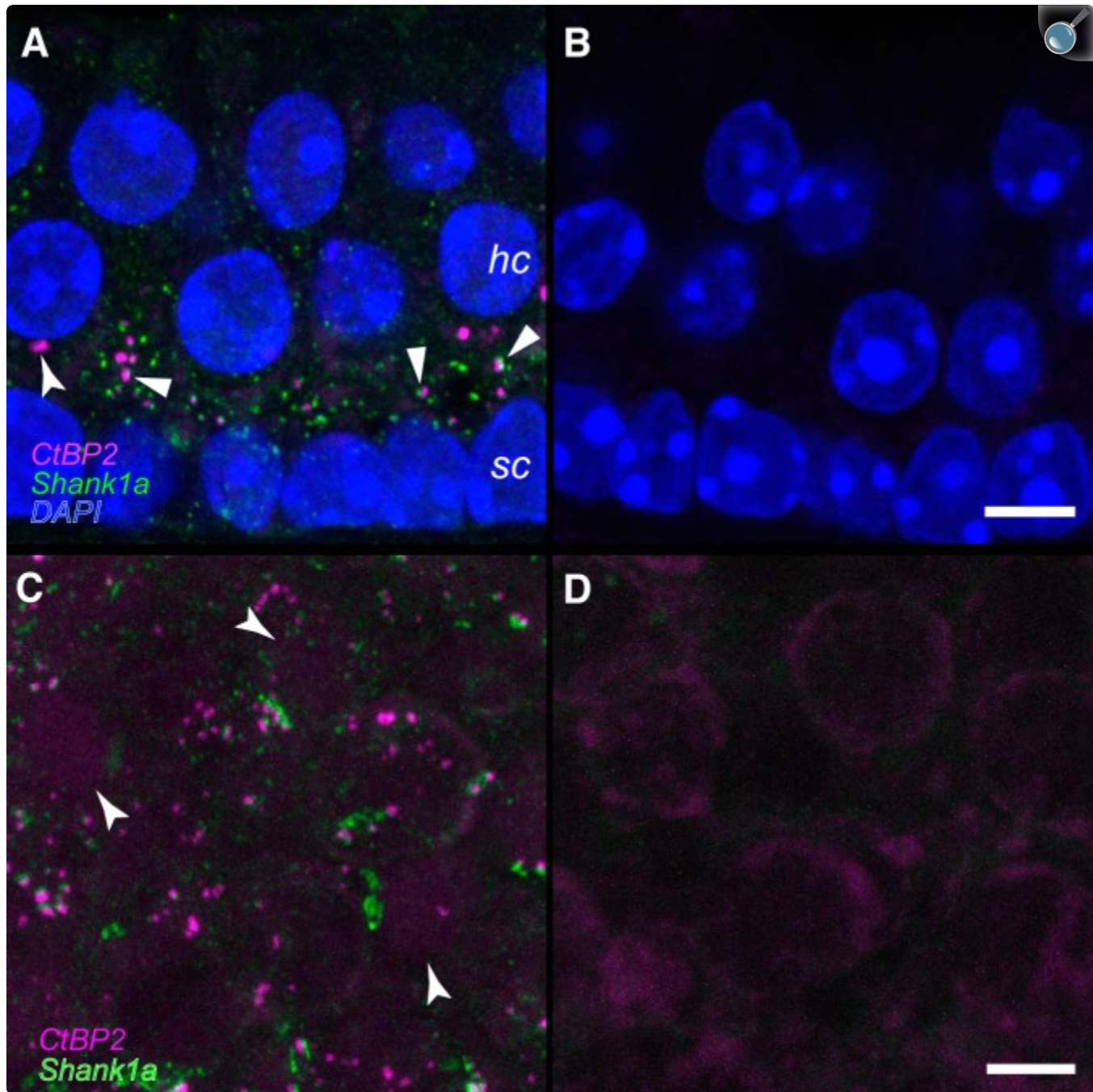
Cellular localization of CtBP2- and Shank1a-positive puncta. These micrographs illustrate closely apposed CtBP2- (red) and Shank1a-positive (green) puncta and provide evidence of their cellular localization in utricles from *thy-1/YFP* mice (Feng et al. 2000). YFP-positive afferent calyces aid in illustrating the spatial localization of synapse markers. *A*: maximum-intensity projection micrograph showing several YFP-positive calyces (grayscale) that encapsulate CtBP2-positive puncta. Additional closely apposed CtBP2- and Shank1a-positive puncta, ostensibly associated with type II hair cells, are readily observed (examples highlighted by white arrowheads). One representative YFP-positive calyx with puncta is isolated (dashed white box) for closer inspection in *B* and *C*. *B*: high-magnification micrograph (single optical section) of the YFP-positive calyx shown in *A*. Shank1a-positive puncta are observed to be spatially close to the calyx, whereas the CtBP2-positive punctum is within the calyx. The dashed white line drawn through the CtBP2 and Shank1a puncta, as well as the calyx, illustrates the dimension of the fluorescence intensity profile shown in *C*. *C*: fluorescence intensity profile from image in *B*, illustrating the overlapping emission from the Shank1a and YFP, whereas CtBP2 exhibits greater spatial segregation. Fluorescence intensity was obtained from a single optical section with 12-bit intensity range and is expressed in fluorescence units (f.u.) These data further support the notion that Shank1a immunolabeling (green) is closely associated with the postsynaptic calyx (grayscale). *D*: mean intensity profiles (f.u.) for 12 CtBP2 (red solid line) and Shank1a (green dashed line) puncta pairs. The respective red- and green-shaded regions reflect the standard deviation of fluorescence intensity profiles. For this analysis, fluorescence intensity profiles from 6 synapses each from 2 image stacks were measured and

aligned on the peak CtBP2 intensity.

Antibody Specificity

Processing controls were conducted in parallel with positive immunostaining experiments to assess nonspecific binding of secondary antibodies and background fluorescence. These were conducted in both cryosections and whole mount specimens, representative results for which are shown in [Fig. 1](#). The cryosections were obtained at 14 µm from an untreated C57Bl/6 utricle after immediate posteuthanasia fixation (as described above) and immersion in 30% sucrose (in PBS) for 12 h. These data are shown in [Fig. 1, A](#) and [B](#). In view of the unique factors required of the BSP processing queue that included a delay of several minutes between euthanasia and specimen fixation, immunostaining controls from additional untreated C57Bl/6 mice were conducted that mimicked this delay. The whole mount control shown in [Fig. 1, C](#) and D, represents a utricle from one of these delayed-fixation controls to illustrate the most realistic case for evaluating immunolabeling and background in the experimental specimens.

Fig. 1.



[Open in a new tab](#)

Verification of antibodies to CtBP2 and Shank1a. *A* and *B*: serial 14- μ m cryosections were obtained from a postnatal day 71 (P71) mouse utricle, and maximum-intensity projections are shown. Hair cell (hc) and support cell (sc) nuclei are illuminated by the DAPI stain (blue). Numerous closely associated CtBP2-and Shank1a-positive puncta can be observed in the positive immunostained section represented in *A* (block arrowheads). The CtBP2-positive puncta highlighted by the flared arrowhead in *A* may represent an undocked

synaptic ribbon. No primary antibodies were included in the processing represented in the micrograph in *B*. The scale bar in *B* represents 5 μm and also applies to *A*. *C* and *D*: maximum-intensity projection micrographs from right and left whole mount utricles from a P65 mouse. Importantly, fixative administration into the temporal bones yielding the specimens represented in *C* and *D* was delayed 7 min to replicate the conditions associated with specimens derived from the microgravity and control specimens. The positive-immunostained specimen of the pair is shown in *C*, where numerous closely associated CtBP2-positive and Shank1a-positive puncta can be observed. Though faint, CtBP2-immunostained nuclei are highlighted by the flared arrowheads. The micrograph in *D* illustrates the results of withholding primary antibodies from the processing. Immunolabeled puncta are not observed. The scale bar in *D* represents 5 μm and also applies to *C*.

The characteristics of positive immunolabeling are represented in the micrographs shown in [Fig. 1](#), *A* and *C*. Nonnuclear anti-CtBP2 immunolabeling with the antibody used in the present study was localized to the basolateral regions in utricular hair cells ([Braude et al. 2015](#); [Sadeghi et al. 2014](#)), and our immunolabeling is consistent with these findings ([Fig. 1A](#)). As expected for an antibody that also recognizes a transcription factor, the anti-CtBP2 also labeled hair cell and support cell nuclei in addition to the puncta consistent with immunolabeled synaptic ribbons ([Fig. 1](#), *A* and *C*) ([Schmitz et al. 2000](#)). A previous investigation showed that the Shank1a antibody used in the present investigation failed to exhibit immunolabeling in utricular epithelia from Shank1 null mice ([Braude et al. 2015](#)), demonstrating the specificity of this antibody for the designated epitope. The secondary-only controls for all antibodies were processed alongside positive immunostaining and illustrate the very low background fluorescence in these specimens ([Fig. 1](#), *B* and *D*), even in the fixation-delayed specimens ([Fig. 1D](#)). These micrographs also illustrate the universal result of absent anomalous immunoreactivity in specimens processed without the addition of primary antibody ([Fig. 1](#), *B* and *D*).

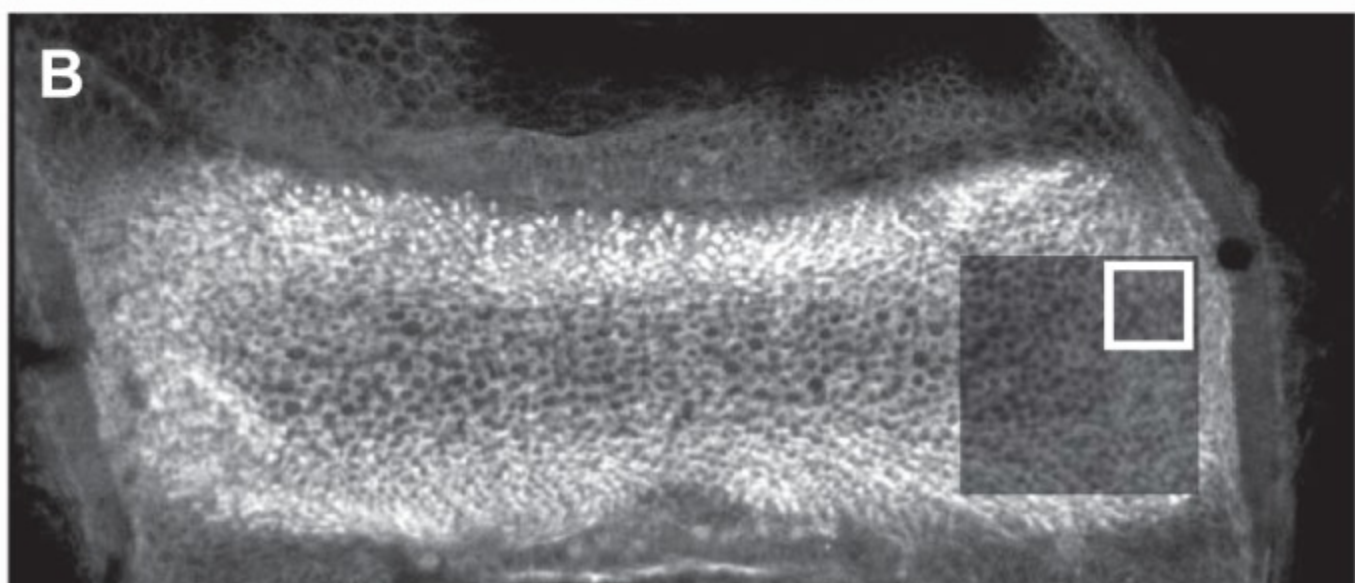
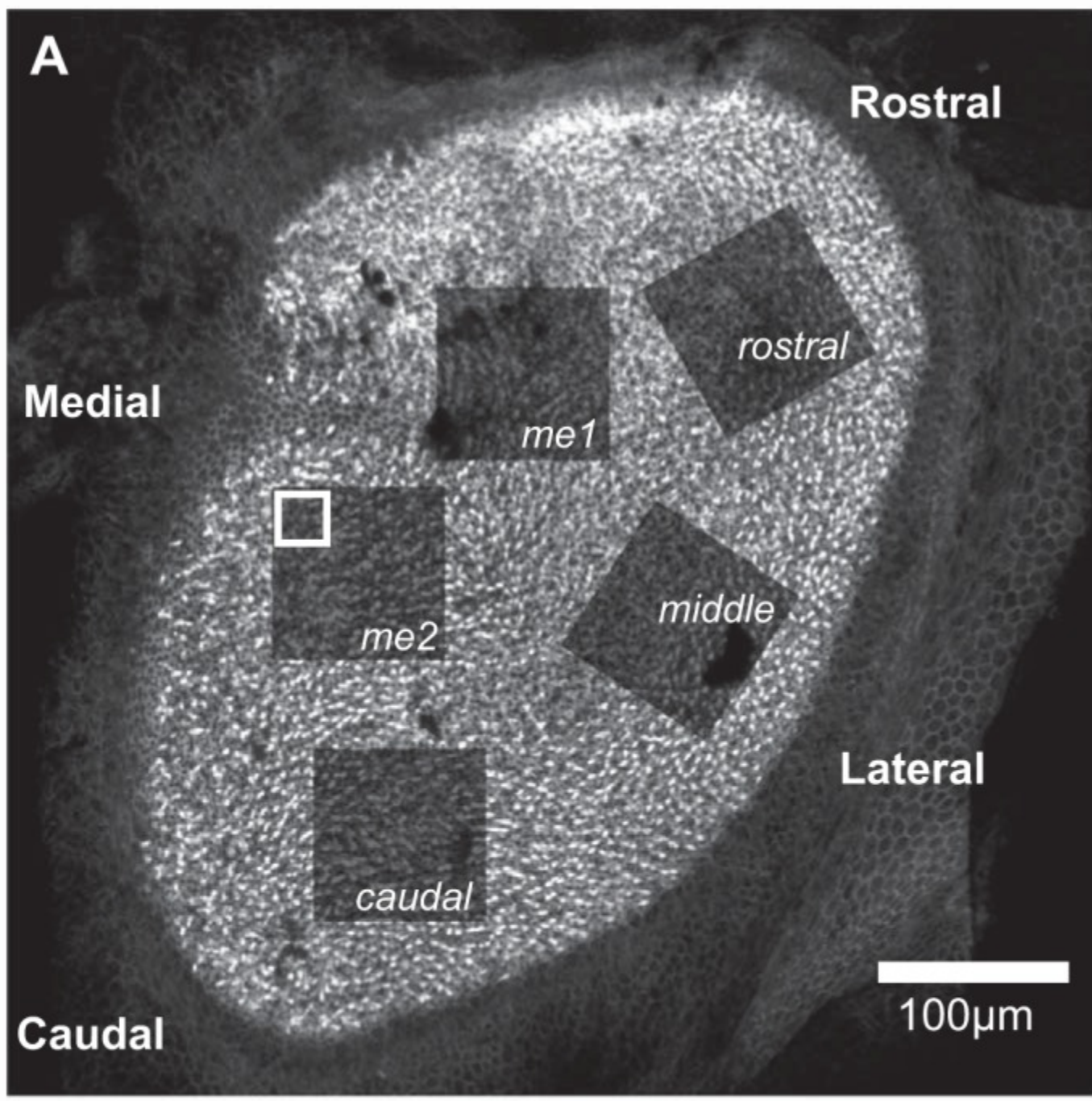
Confocal Imaging and Synapse Quantification

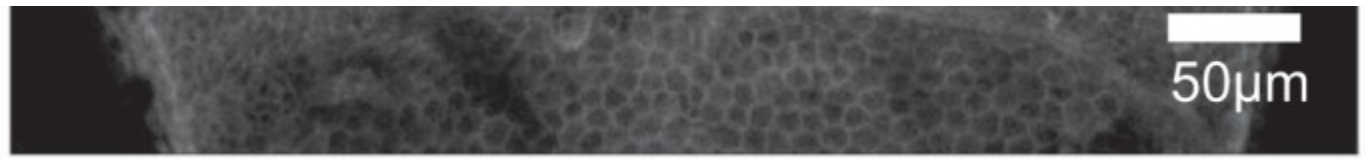
Confocal images were captured on a Zeiss LSM 510 Meta confocal microscope implemented on an upright Axioplan 2 microscope with the use of Zeiss LSM 510 software. The 488-nm (15% intensity), 543-nm (80–100% intensity), and 633-nm (10–20% intensity) laser lines were used for excitation. Bandpass filters (standard filter set of the Zeiss LSM 510 Meta) of 505–530 and 560–615 nm and a long-pass filter of 650 nm were used to capture separate emission channels. A Zeiss Plan-Neofluar ×10/0.3-NA objective was used to capture low-magnification images, and high-magnification images were obtained using a Zeiss Plan-APOCHROMAT ×63/1.4-NA oil-immersion objective. In this image acquisition configuration, the pinhole sizes were 50, 56, and 65 μm for the 488-, 546-, and 633-nm excitation lines, respectively. The optical section thickness was 0.37 μm. The overall *x-y* scan size was 1,000 × 1,000 pixels, whereas the total stack depth depended on factors such as epithelial region and the degree to which the specimen laid flat on the microscope slide. A sufficient number of optical sections were collected to image from the epithelial surface through the support cell layer. Maximum-intensity projection micrographs from selected confocal stacks were prepared for publication using Volocity software (PerkinElmer, Waltham, MA). Adobe Photoshop 7.0.1 (Adobe Systems, San Jose,

CA) was used to compile micrographs.

Images were systematically acquired for each utricle to sample two regions ($90 \mu\text{m} \times 90 \mu\text{m}$) from the medial extrastiola, three regions from the striola, and one region from the horizontal crista planum ([Fig. 2](#)). Manual synapse counting was made more manageable by parsing each acquired image stack into three smaller substacks, each with a two-dimensional (2-D) optical section surface area of $900 \mu\text{m}^2$ ($30 \mu\text{m} \times 30 \mu\text{m}$), using Volocity image analysis software. These smaller volumes were easily analyzed within one 2- to 3-h block without risking fatigue and concomitant errors on the part of the observers. At the same time, this strategy of quantifying multiple substacks strengthened the data set by subjecting a substantial fraction of the original image stack for analysis. The cropped image stacks were used for all analyses without further filtering. Image acquisition strategies and sampling were performed for different regions of the utricle and the horizontal cristae by using the following approaches.

Fig. 2.





[Open in a new tab](#)

Topography-based confocal imaging of mouse vestibular epithelia. The locations of image stacks acquired from utricles and horizontal cristae are illustrated by the photobleached areas in specimens labeled with fluorophore-conjugated phalloidin. These appear as areas of diminished fluorescence after image stack acquisition. The white boxes represent the area of the 30- μm \times 30- μm substack that was extracted from the larger image stack for the purpose of synapse counting. *A*: 5 regions of the mouse utricle were imaged for quantitative synapse analysis. These regions correspond to the utricular topography as follows: me1 and me2, medial extrastriola; caudal, caudal striola; middle, middle striola; and rostral, rostral striola. *B*: the planum of the horizontal crista (indicated by the absence of cruciate eminence featured in the superior and posterior cristae) was imaged for synapse quantification, illustrated by the postimaging photobleached area shown, and served as within-specimen control epithelium that is gravity insensitive.

Utricle medial extrastriola.

From the two raw image stacks, substacks used for quantification were selected as random, nonoverlapping regions. These cropped substacks, three from each of the larger raw image stacks (for a total of 6 substacks), were used for synapse and hair cell quantification for this topographical region of each utricle.

Utricle striola.

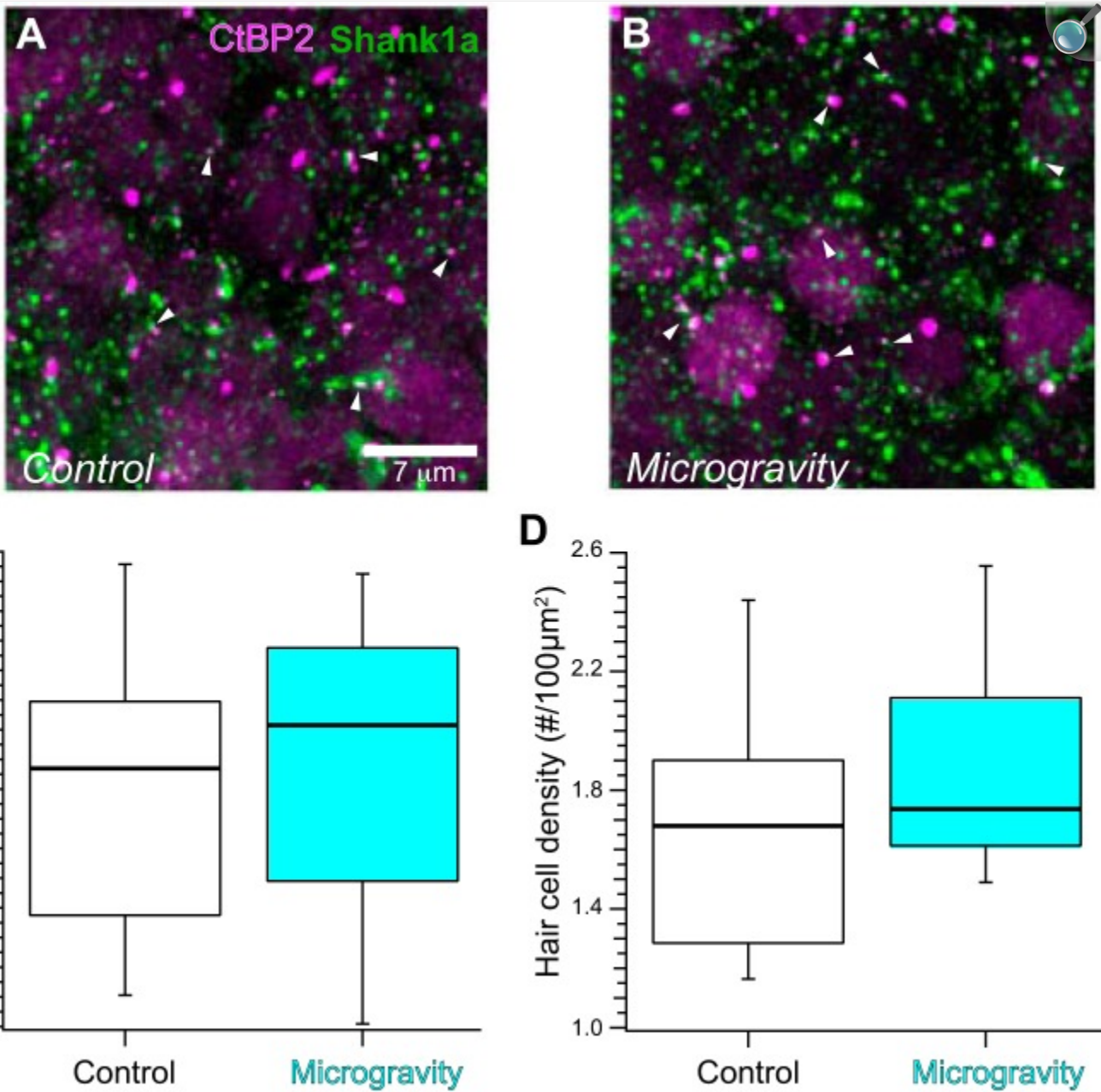
Three raw image stacks were acquired representing the rostral, middle, and caudal portions of the striola. Image analyses were performed on nonoverlapping substacks that were cropped medial to the line of polarity reversal (LPR). A total of nine cropped regions (3 regions each from the rostral, middle, and caudal image stacks) were used for synapse and hair cell quantification.

Horizontal crista.

One image stack was obtained from the apical portion of the planar expansion (i.e., the planum semilunatum) of each horizontal crista. Image analyses were performed on nonoverlapping image stacks that were cropped from the apical-most region of the mounted crista. Three cropped image stacks were used to count synapses and hair cells for each crista.

Two observers, blinded to any identifying characteristic of each image stack (i.e., epithelial region and gravity condition), counted synapses and hair cells. Synapses were identified and marked within the epithelia volume that ranged in depth from the top of type II hair cell nuclei to the support cell nuclei. We defined a synapse for quantification as close apposition of both pre- and postsynaptic markers (CtBP2 and Shank1a, respectively; [Figs. 3–6](#)). The number of hair cells was quantified by the phalloidin-stained apical surface of the sensory epithelium. Hair cells were identified by phalloidin-stained stereocilia at the epithelial surface, which collectively represented “counting units.” We followed a well-established stereological convention to accommodate “partial” counting units ([Gundersen 1977](#); [Mayhew 1996](#)). This convention specifies that a counting frame be implemented whose edges define the area within which objects of interest are counted. In our case this frame is established by the square area of confocal scanning. Two adjacent edges are “forbidden,” and counting units (e.g., phalloidin-stained stereocilia bundles) transected by these edges are not counted, whereas those transected by the opposite edges are counted.

Fig. 6.



[Open in a new tab](#)

Synapse distribution in confocal stacks from control and microgravity horizontal cristae. *A* and *B*: maximum-intensity projection micrographs representing optical sections from planar region confocal stacks in immunolabeled control (*A*) and microgravity (*B*) horizontal cristae. Synapses defined as closely apposed CtBP2- and Shank1a-positive puncta are observed throughout the micrographs, without apparent differences in synapse densities in control and microgravity specimens. *C*: the synapse densities in control and microgravity horizontal cristae were found to be similar, as illustrated in the box-and-whisker plots. *D*: hair

cell densities were also found to be similar in control and microgravity specimens.

Statistical Analyses

We implemented a linear mixed-effects model in the R statistical computing environment ([Bates et al. 2015](#); [R Development Core Team 2012](#)) to evaluate the fixed factor of gravitational status (i.e., control or microgravity) on two measures of synapse densities: closely apposed puncta per $100 \mu\text{m}^2$ epithelial surface area and closely apposed puncta per hair cell. We also conducted parallel analyses on hair cell densities (hair cells per $100-\mu\text{m}^2$ epithelial surface area). This model was applied to synapse density measures from the medial extrastriola, striola, and horizontal crista. The model included factors for which measures were not independent (i.e., so-called random effects; analyzing fixed and random effects together represents a mixed model), which included analyses from the three substacks from the same larger region, regions of epithelia (e.g., utricle and horizontal crista) from the same specimen, and analyses conducted by the two observers on the same image stacks. The linear mixed-effects model accounts for the nonindependent measures (i.e., it effectively applies a repeated-measures design). A bootstrap resampling design was implemented to test hypotheses stipulating that the measures of synapse densities and hair cell densities in microgravity-exposed specimens were similar to the Earth-gravity control specimens. This enabled generation of F -statistic distributions that were based on random resampling of the data collected from these experiments and computation of explicit probabilities that the F statistics resulting from the empirical data distributions could have resulted from random sampling from all of the density measures. For analyses of the medial extrastriola and horizontal crista, hypothesis testing was restricted to a single fixed-effect factor, gravitational status, that included only two levels (control and microgravity). Therefore, multiple comparison tests were not necessary to determine statistical similarities beyond analyses of the F statistic. For each comparison, the empirical and critical value F statistics are provided, the latter designated at the probability p ($F_{c,p}$). In all but one case, explicit probabilities were determined from the distribution of F statistics resulting from ANOVA calculations following bootstrap resampling of 100,000 resampling trials.

Implementation of the linear mixed model for all striolar data included region (i.e., rostral, middle, and caudal; see [Fig. 2A](#)) as a fixed effect as well as a random effect (to account for nonindependent measures stemming from 3 regions taken from each specimen). The striolar regions represented spatially different areas of the utricle, and therefore it was deemed prudent to evaluate synapse and hair cell density measures from each region rather than pooling over this factor. In addition, the caudal region of striolae from our mouse utricles was most similar to the region analyzed in the previous ultrastructural analyses from the posterior rat utricle ([Ross 2000](#)). Therefore, more direct comparisons were derived by maintaining spatial identity of striolar regions analyzed in the present study, and Tukey multiple comparison tests were implemented for the pairwise comparisons. Within the framework of our linear mixed-effects model, Tukey tests were executed through the `glht` function library in R. In these cases, all degrees of freedom were not available and t statistics (generally associated with Tukey multiple comparisons) could not be computed. Rather, “ z ” statistics were specified with corresponding P values, which are reported for corresponding statistical results.

RESULTS

Topographical Sampling

The strategy for imaging whole mounted utricles is illustrated in [Fig. 2A](#), representing a control specimen stained with fluorophore-conjugated phalloidin to illuminate the stereocilia at the apical surface of the epithelium. The darkened regions represent the photobleaching that was achieved during confocal imaging of the stereocilia and provided an unambiguous record of the regions imaged for each utricle. The regions labeled me1 and me2 represent the medial extrastriola, whereas the striola regions are labeled caudal, middle, and rostral corresponding to their relative topographic location. Similarly, [Fig. 2B](#) exemplifies the image sampling of the horizontal crista planum. It is important to note that whereas the acquired striolar confocal volumes included hair cells lateral to the line of polarity reversal (LPR), substacks created for analysis from these larger volumes only included hair cells medial to the LPR, which was easily located in these specimens by virtue of the phalloidin labeling. Therefore, these analyses encompassed the striola, defined as the utricular region harboring calretinin-positive afferent calyces, which are almost exclusively medial to the LPR ([Li et al. 2008](#); [Schweizer et al. 2009](#)).

Association of Shank1a with CtBP2

The data in [Fig. 3](#) illustrate the close association between presynaptic CtBP2- and postsynaptic Shank1a-immunolabeled puncta. We utilized vestibular epithelia from the Y16 line of transgenic mice ([Feng et al. 2000](#)) to analyze the spatial apposition in greater detail. In these specimens YFP was robustly expressed in afferent neurons projecting to the vestibular epithelia, terminating in several YFP-positive calyces (grayscale) illuminated in [Fig. 3A](#). Prominent among these is the calyx highlighted within the dashed box, within which is a large CtBP2-positive punctum closely apposed to a cluster of Shank1a-positive puncta. This calyx and associated immunolabeled puncta are shown at higher magnification by the single optical section in [Fig. 3B](#), illustrating the relative spatial relationship between immunolabeled puncta and intrinsic calyceal YFP fluorescence. The fluorescence intensity profiles along a line segment (dashed), drawn through the anti-CtBP2 and anti-Shank1a puncta, as well as the YFP-labeled calyx, are plotted in [Fig. 3C](#). The emission profiles of anti-Shank1a (green) and the postsynaptic calyx (gray) exhibit considerable overlap indicative of their colocalization; this finding is consistent with Shank1a being a receptor scaffold protein within the postsynaptic plasma membrane ([Braude et al. 2015](#)). The peaks of both the YFP and Shank1a emission profiles were at a greater distance to the CtBP2 emission profile than to one another, consistent with the presynaptic location of CtBP2 within the hair cell. The distance between peak fluorescence of CtBP2- and Shank1a-immunolabeled puncta is ~1 μ m.

Further analyses of emission profiles exhibited by closely apposed CtBP2 and Shank1a puncta are illustrated in [Fig. 3D](#). Profiles of 13 puncta pairs were obtained from single optical sections of two independent confocal stacks in a manner similar to that demonstrated in [Fig. 3](#), B and C. The intensity profiles of the CtBP2 puncta were aligned, from which the

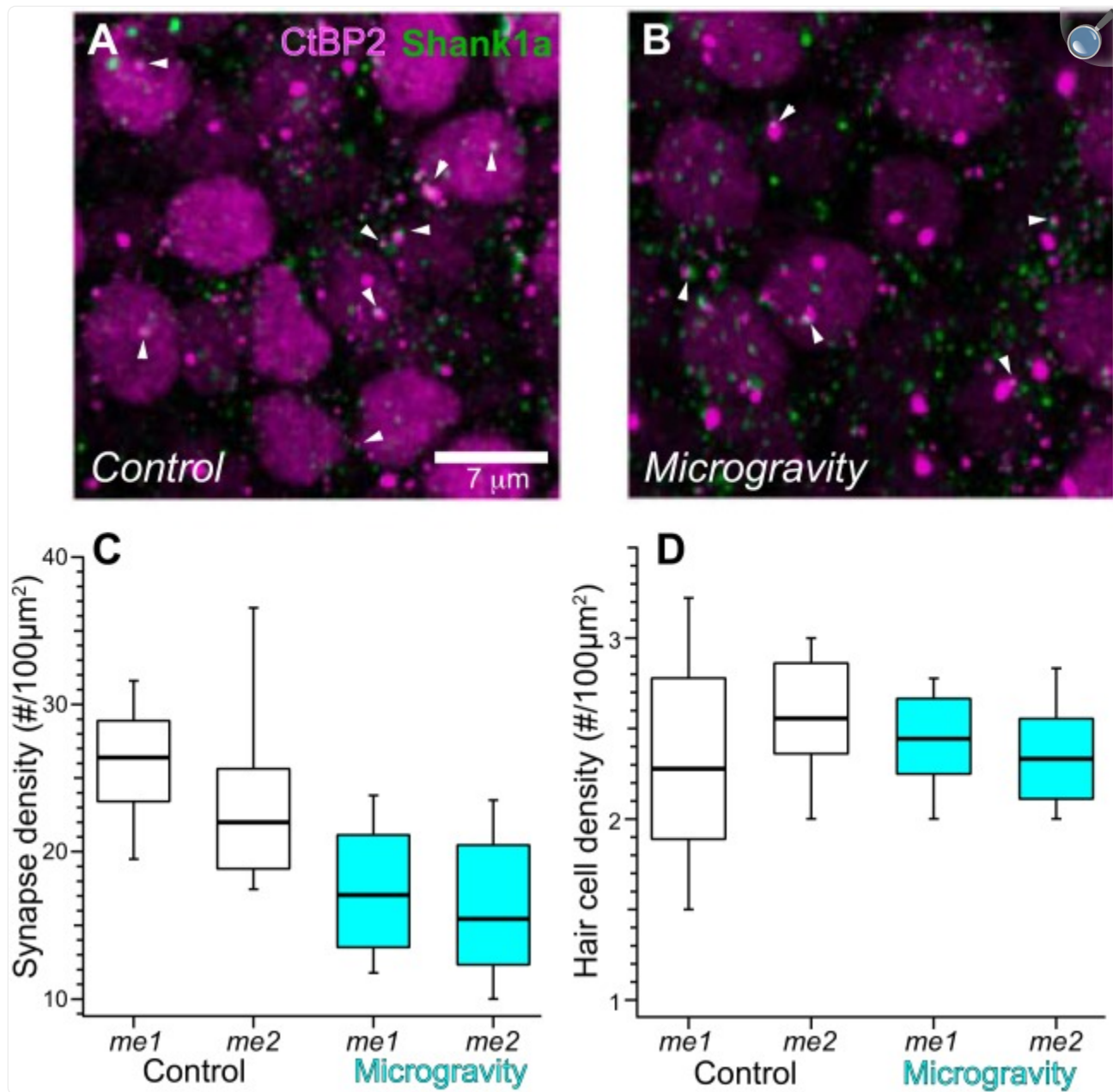
relative distance of each corresponding Shank1a punctum was determined. [Figure 3D](#) shows the mean fluorescence emission profile for all 13 puncta pairs (red solid and green dashed lines); the shaded regions represent the standard deviation of the mean emission for each channel along the profile path. These data illustrate that although the example profiles in [Fig. 3, B](#) and [C](#), exhibited a peak-to-peak distance of ~1 μm , the distances between mean fluorescence intensity peaks in these examples are much closer at ~0.3 μm . The key conclusion from these data is that the fluorescence emission profiles of Shank1a-positive puncta are consistent with Shank1a being an affirmative marker of the postsynaptic receptor complex in the mammalian utricle. The “close apposition” to CtBP2 exhibits some heterogeneity in distance. Furthermore, it is important to remember that utricular hair cell synaptic ribbon can extend considerably into the cytoplasm, and the CtBP2 signal is thus not expected to be as close to the presynaptic membrane as presynaptic markers are at conventional synapses.

Synapse Densities in the Medial Extrastriola Exhibited Spaceflight-Induced Plasticity

Analysis of the medial extrastriola was conducted in two larger image volumes as shown in [Fig. 2A](#) (e.g., regions labeled me1 and me2). The objective of this sampling paradigm was to increase the area of medial extrastriola neuroepithelium that was analyzed; we had no a priori rationale for testing hypotheses regarding differential synaptic plasticity in specific medial extrastriolar loci (i.e., me1 vs. me2). Therefore, substack identity with respect to its larger original image stack was retained in the final analysis for the sole purpose of accounting for the repeated measures design (i.e., nonindependence of substacks parsed from the same larger image stack, and therefore the data was obtained using identical imaging parameters).

The distributions of CtBP2- and Shank1a-positive puncta within individual medial extrastriolar confocal substacks are illustrated in the maximum-intensity projection micrographs from control and microgravity-exposed utricles in [Fig. 4, A](#) and [B](#), respectively. These micrographs provide a snapshot of labeled synapses imaged in whole mounted specimens, in which they are abundantly seen as closely associated CtBP2 (red)- and Shank1a (green)-immunolabeled puncta. Nuclei of hair cells are also visualized by virtue of positive anti-CtBP2 immunolabeling. The distributions of synapse densities, expressed as count per 100 μm^2 , are depicted by the box-and-whisker plots in [Fig. 4C](#). As described in METHODS, our implementation of the linear mixed-effects analytical model stipulated gravity condition as the sole fixed effect factor (2 levels, control and microgravity) and three additional random effects factors to account for measurement nonindependence. These random effects factors were region (measures from 3 substacks from each of 2 regions of medial extrastriola), specimen (2 regions from the same utricle), and observer (*observers A* and *B*; although their activities were independent and blinded to stack identity, they analyzed the same confocal stacks). The analysis accounts for the measurement variance due to the nonindependent random effects factors while quantifying the measurement variance due to gravity status (the fixed effect factor). The box-and-whisker plots illustrate synapse density distributions associated with control and microgravity conditions in the two medial extrastriola regions (labeled me1 and me2).

Fig. 4.



[Open in a new tab](#)

Synapse distribution in confocal stacks from the medial extrastriola in control and microgravity utricles. *A* and *B*: maximum-intensity projection micrographs of medial extrastriola confocal stacks from immunolabeled control (*A*) and microgravity utricles (*B*). Synapses defined as closely apposed CtBP2- and Shank1a-positive puncta (examples highlighted by white arrowheads) are observed throughout the micrographs. *C*: box-and-whisker plots representing the distributions of synapse densities (synapse count per $100\ \mu\text{m}^2$, normalized to surface area of confocal stack) in the 2 medial extrastriola regions (i.e., me1 and me2, [Fig. 2A](#)), illustrating the

decreased synapse densities found in medial extrastriolae from microgravity specimens. *D*: box-and-whisker plots of hair cell densities in the two medial extrastriolar regions from control and microgravity specimens. These data and associated linear mixed model analyses illustrate the similarity in medial extrastriola hair cell distributions in both conditions, indicating that the differences in synapse densities cannot be explained by microgravity-induced alterations in hair cell density.

The outcome of testing the null hypothesis via the linear mixed-effects model ANOVA, stipulating that synapse densities (as synapses per $100 \mu\text{m}^2$) were similar in measures associated with control and microgravity conditions, is clearly shown in [Fig. 4C](#). This hypothesis was soundly rejected ($F = 17.69$; $F_{c,0.0001} = 15.91$; $P = 0.000032$). From this analysis we conclude that synapse densities in medial extrastriola hair cells decreased with a 15-day exposure to microgravity. In comparing the median values across gravity condition, this decrease amounted to 32.6%.

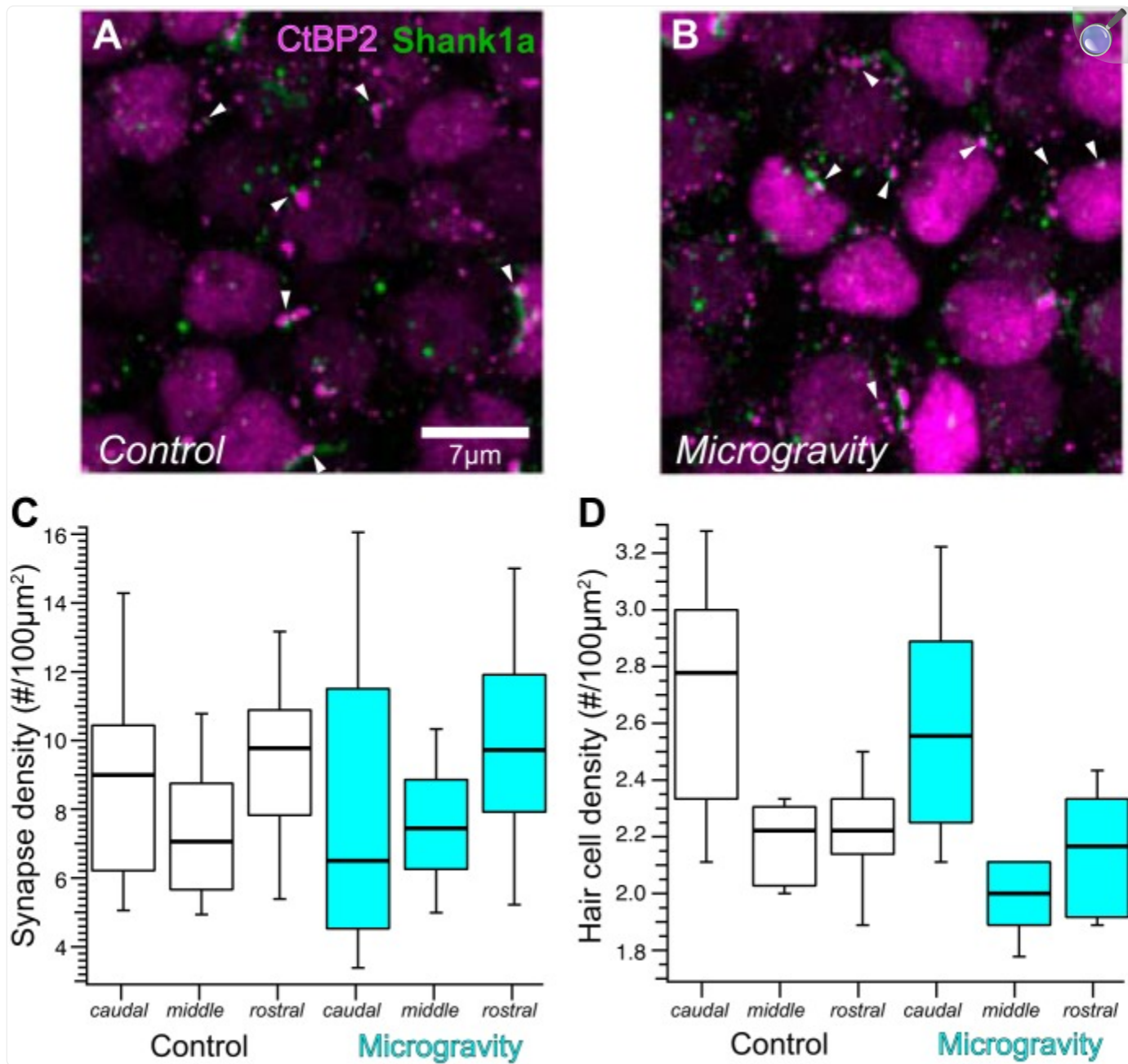
Hair cell densities in the mouse utricle and crista exhibit considerable heterogeneity across the topography of the epithelia, and therefore we analyzed this parameter in each substack. This analysis would serve as a control for heterogeneities in hair cell distributions across epithelial region that could contribute to synapse density. The results are illustrated by the box-and-whisker plots in [Fig. 4D](#). We implemented an identical linear mixed-effects analytical model to test the hypothesis that hair cell densities were similar in measures obtained from control and microgravity specimens. The analysis supported this null hypothesis ($F = 0.13$; $F_{c,0.05} = 3.83$; $P = 0.71$), which indicated that the decrease in synapse density found in the medial extrastriola from microgravity-exposed utricles could not be explained by concomitant changes in hair cell density.

Unchanged Synapse Densities in the Utricular Striola Reflect Topography-Dependent Plasticity

To determine whether the spaceflight-induced modifications in synapse density exhibited in the medial extrastriola were manifested generally across the topography of the utricle, we analyzed synapse densities in the three striolar regions from control and microgravity utricles. These regions correspond to caudal, middle, and rostral areas as identified in [Fig. 2A](#). [Figure 5](#), *A* and *B*, represents maximum-intensity projections from middle confocal stacks of control ([Fig. 5A](#)) and microgravity-exposed ([Fig. 5B](#)) utricles. The numerical distributions of synapse density in the three striolar regions are shown in [Fig. 5C](#). Through the bootstrapped linear mixed-effects ANOVA, we tested whether synapse densities were similar in control and microgravity specimens (main gravity condition effect) and across the three striolar regions (main region effect). The analytical design also tested for interaction between the two main effects, which would identify synapse density differences between control and microgravity specimens in only one or two specific regions. The null hypothesis was supported for the main gravity condition effect, demonstrating that synapse densities were similar for control and microgravity conditions ($F = 0.035$; $F_{c,0.05} = 3.91$; $P = 0.85$), as well as the interaction between gravity

status and striolar region ($F = 1.14$; $F_{c,0.05} = 3.25$; $P = 0.37$). However, this analysis did reveal differences in synapse density across striolar regions (main region effect; $F = 8.10$; $F_{c,0.001} = 7.76$; $P = 0.00074$). Application of the Tukey multiple comparison test indicated that synapse density within the middle striolar region was less than in both the rostral ($z = 2.77$; $z_{c,0.05} = 2.34$; $P = 0.016$) and caudal regions ($z = 2.50$; $z_{c,0.05} = 2.34$; $P = 0.034$), whereas densities in rostral and caudal striolar regions were similar ($z = 0.21$; $z_{c,0.05} = 2.34$; $P = 0.98$). In summary, these data demonstrate that although synapse densities are not homogeneous across striolar regions, spaceflight did not induce further changes in synapse density within the utricular striola. This further indicates that the structural plasticity found in the medial extrastriola of microgravity utricles (Fig. 4) is not homogeneous across the topography of the utricle.

Fig. 5.



[Open in a new tab](#)

Synapse distribution in striolar regions of control and microgravity utricles. *A* and *B*: maximum-intensity projection micrographs representing confocal stacks from middle striolar regions in immunolabeled control (*A*) and microgravity utricles (*B*). Closely apposed CtBP2- and Shank1a-positive puncta (examples highlighted by white arrowheads) are observed throughout the micrographs. Synapses are clearly less dense in these striolar micrographs compared with those from medial extrastriola (Fig. 4). *C*: box-and-whisker plots of synapse densities (synapse count per $100 \mu\text{m}^2$) in caudal, middle, and rostral (Fig. 2A) striolar regions of

control and microgravity specimens. Synapse densities in the striola were similar among all specimens regardless of gravitational condition. *D*: hair cell densities (hair cell count per $100 \mu\text{m}^2$) among the 3 striolar regions in control and microgravity specimens are illustrated in box-and-whisker plots. Hair cell densities across gravitational condition were similar.

The outcome of hair cell density measurements was similar to that found for synapse density, indicating similarities in hair cell density across gravity condition ($F = 0.13$; $F_{c,0.05} = 3.82$; $P = 0.71$) and supporting the interaction of gravity condition and striolar region ($F = 0.50$; $F_{c,0.05} = 3.23$; $P = 0.62$). However, hair cell densities across regions were heterogeneous, whereby hair cell density was higher for the caudal striola compared with the rostral ($z = 6.10$; $z_{c,0.05} = 2.91$; $P < 0.0001$) and middle regions ($z = 6.99$; $z_{c,0.05} = 2.91$; $P < 0.0001$), whereas densities in the middle and rostral regions were similar ($z = 0.91$; $z_{c,0.05} = 2.34$; $P = 0.64$).

Synapse Quantification in the Horizontal Crista Planum Tests for Gravity Nonspecific Modifications

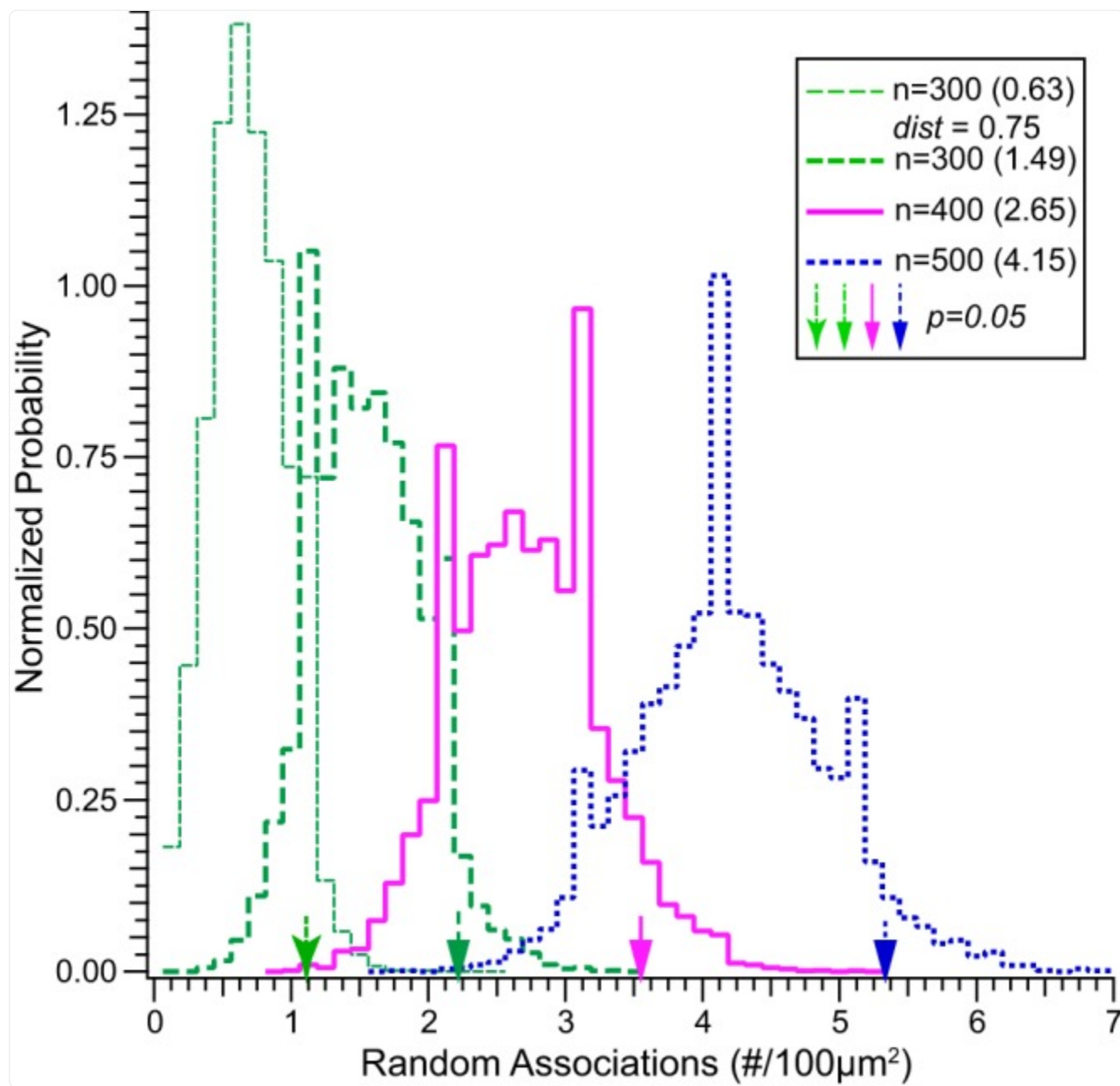
The horizontal cristae from control and microgravity specimens were also analyzed in the present study as “within-subject” controls. We proposed that the changes in synapse density in microgravity-exposed utricular epithelia were induced by the conditions of gravitational unloading concomitant with spaceflight. It was important to consider the alternative that the changes could be induced by alterations in environmental conditions imposed by spaceflight but not specifically associated with the gravitational unloading, such as general systemic stress, radiation exposure, or other unknown factors. If synaptic modifications were induced by factors not specifically associated with alterations in ambient gravity but generally affected labyrinthine sensory epithelia, then a high probability existed that these factors would affect the semicircular canal cristae, as well. Analysis of crista epithelia served as a test of this possibility.

The results from analyses of horizontal crista epithelia are shown in [Fig. 6](#), showing CtBP2- and Shank1a-immunolabeled puncta in maximum-intensity projections of representative confocal micrographs ([Fig. 6, A and B](#)) and a box-and-whisker plot ([Fig. 6C](#)). Similar to the strategy for the utricular regions, we tested the hypothesis that synapse densities in horizontal cristae were similar in control and microgravity-exposed conditions. Using bootstrap linear mixed-effects ANOVA, we found that this hypothesis was supported ($F = 0.072$; $F_{c,0.05} = 4.05$; $P = 0.79$), and therefore we conclude that synapse density is unchanged in the horizontal crista after spaceflight. Hair cell densities were also determined in the planar region substacks from control and microgravity horizontal cristae and are plotted in [Fig. 6D](#). Linear mixed model ANOVA analyses revealed that these densities were similar ($F = 1.67$; $F_{c,0.05} = 4.11$; $P = 0.20$).

Simulations of Random Associations Between Puncta in a Confocal Volume

The present study incorporated a strategy of quantifying synapses defined as closely apposed pre- and postsynaptic puncta within “volumes” from various topographic regions of utricular and crista epithelia obtained from microgravity and control mice. Furthermore, the data from [Fig. 3](#) illustrate that the inter-punctum distance for such “close apposition” could be as large as 1 μm when analyzed via confocal microscopy. We sought to glean some perspective for these synapse counts by evaluating the probability of random close appositions between pre- and postsynaptic puncta within 1 μm of one another. This was achieved by conducting simulations in which two populations of markers were independently and randomly distributed in a cubic volume measuring 30 μm in height, width, and depth. The resolution of each dimension was 30 nm (i.e., 1,000 points along each dimension), producing a total of 10^9 possible vertices (i.e., x, y, z coordinate locations) for random spatial distribution. This volume and possible locations were similar to the confocal volumes analyzed in the present investigation. Simulations were conducted for populations numbering 300, 400, and 500 puncta per marker (2 markers per simulation) based on counts of ~300–500 total CtBP2-positive puncta in the confocal stacks analyzed in the present study. For each simulation, counts of closely apposed puncta (i.e., one from each population within 1 μm) were determined. The simulation was repeated 10,000 times for each population quantity, the results of which are shown in [Fig. 7](#). An additional simulation was conducted for puncta populations of 300 per population, for which the distance criterion was reduced to 0.75 μm . All simulation data are expressed as random association counts per 100 μm^2 for direct comparison with the empirical synapse data in [Figs. 4–6](#).

Fig. 7.



[Open in a new tab](#)

Simulations reveal the probability of random associations between 2 “virtual markers” within a volume. Histograms represent the distribution of 2 closely apposed (i.e., $\leq 1 \mu\text{m}$) markers, 1 from each of 2 virtual populations, expressed as count per $100 \mu\text{m}^2$ and conforming to the analyses reflected in [Figs. 4–6](#). The 2 virtual populations were randomly distributed in a cubic volume with x , y , and z dimensions of $30 \mu\text{m}$ and a resolution of 30 nm (1,000 points along each dimension). Each histogram reflects the distributions of random association within $1 \mu\text{m}$ between the 2 marker populations, numbering 300 (green thick dashed line), 400 (red

solid line), and 500 (blue dashed line) for each marker. The mean number of random associations is reflected in parentheses within the key, and the count representing 5% probability for each distribution is indicated by the respective vertical arrows. Counts corresponding to the 1% probability for each distribution are 2.56 ($n = 300$), 4.0 ($n = 400$), and 5.78 ($n = 500$). The histogram at the *far left* (green thin dashed line) represents the distribution of random associations within 0.75 μm to illustrate the decreased probability as the distance criterion decreases. As shown in [Fig. 3](#), many CtBP2 and Shank1a puncta are much closer than 1 μm .

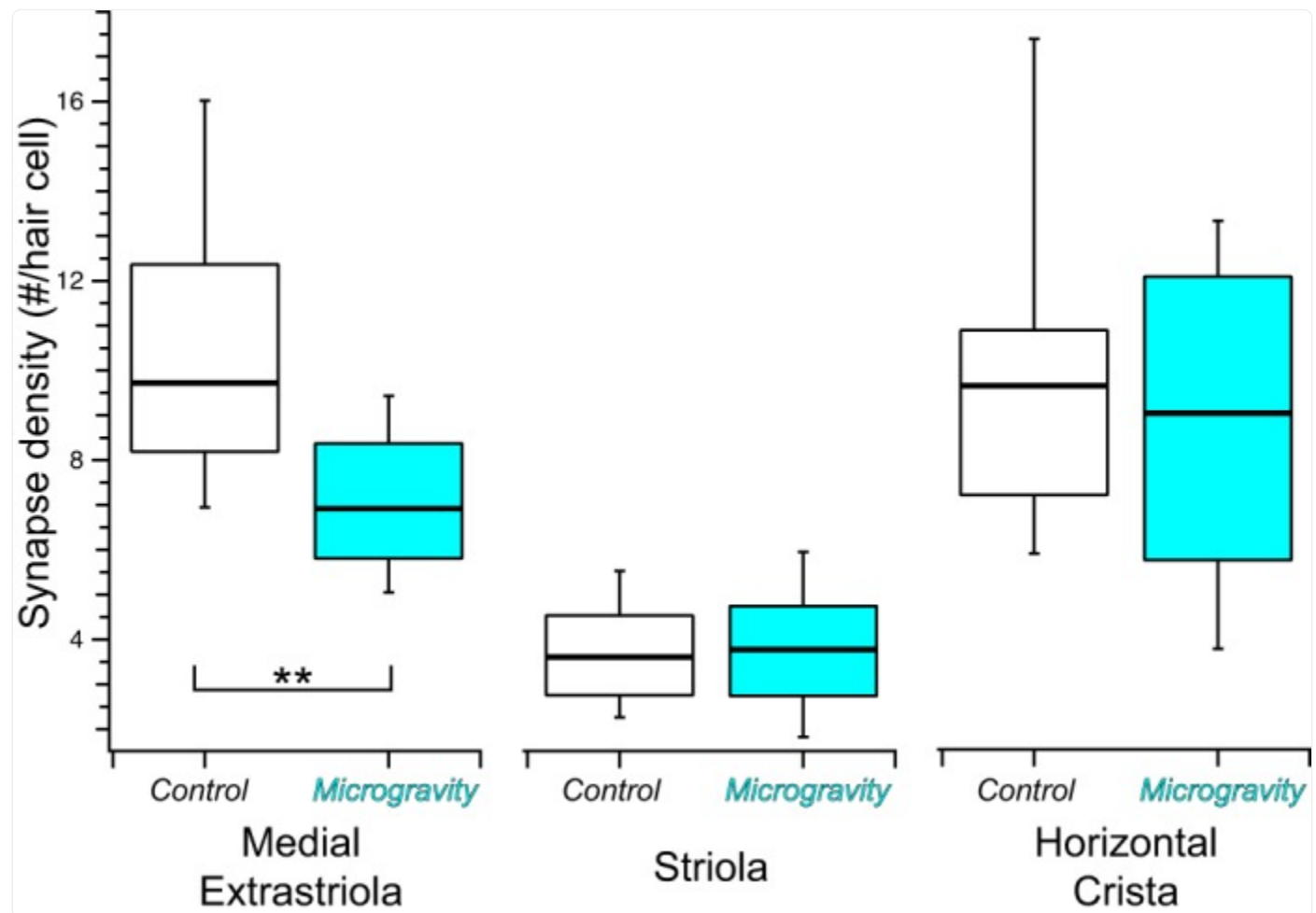
Despite 10^9 possible locations for each marker (i.e., 1,000 possible coordinates along each of 3 axes for a defined volume), these simulations demonstrate that the probability of a random association between members from each marker population (i.e., $n = 300$, 400, or 500 each, within 1 μm) is larger than might be expected. Consider the simulation in which random associations within 1 μm were counted for two marker populations numbering 300 each (green thick dashed line). This simulation demonstrated a 5% probability (i.e., $\alpha = 0.05$) of a random association count of 2.2 per 100 μm^2 (indicated by the green block arrow along the abscissa). For the populations numbering 400 (red solid line) and 500 (blue dashed line), the random association counts at $\alpha = 0.05$ were 3.6 (red block arrow) and 5.3 (blue block arrow) associations per 100 μm^2 , respectively. It is important to note that these associations are purely random and without any spatial specificity, whereas the immunolabeled puncta were certainly not random (i.e., immunolabeled puncta not observed in controls in which primary antibodies were withheld from processing). Furthermore, [Fig. 3D](#) illustrates that the distance between many CtBP2 and Shank1a associations was far less than 1 μm . Therefore, an additional simulation was conducted to evaluate the influence of narrowing the distance criterion on the probability of random associations. For this simulation, the distance criterion was narrowed to 0.75 μm , whereupon the probability of random association decreased as illustrated by the histogram at *far left* in [Fig. 7](#) (green thin dashed line). With narrowing of the distance criterion, the random association count associated with 5% probability was reduced to just over 1 “virtual synapse” per 100 μm^2 (green flared arrow, *far left* along abscissa). Very similar results were obtained when we simulated random distributions in 3-D volumes and measured the nearest distance between points of two distinct distributions. Therefore, although we cannot exclude the possibility of random association between CtBP2- and Shank1a-immunolabeled puncta, the probabilities of occurrence were low.

Synaptic Plasticity

The analyses presented thus far demonstrate an overall decrease in synapse density within the medial extrastriolae of utricles from microgravity-exposed mice, expressed as synapse count per 100 μm^2 of epithelia surface area. These changes were specific to this region of sensory epithelia, since synapse density modifications were not observed in the striolae or horizontal cristae. Because hair cell density is not uniform across all epithelial regions, we also analyzed synapse density normalized to hair cell density to further scrutinize synapse density modifications across sensory epithelia. These data are shown by the box-and-whisker plots in [Fig. 8](#) for the medial extrastriola and striola regions of the utricle and for the horizontal crista planum. Consistent with the previous analyses, the linear mixed-effects model

ANOVA revealed that synapse densities expressed as synapses per hair cell were similar in control and microgravity conditions for both the striola ($F = 0.036$, $F_{c,0.05} = 3.91$; $P = 0.85$) and horizontal crista ($F = 0.54$, $F_{c,0.05} = 4.03$; $P = 0.48$). However, synapse density per hair cell decreased in the medial extrastiola as a result of microgravity exposure ($F = 9.02$, $F_{c,0.005} = 7.95$; $P = 0.0027$). This additional analysis supports the conclusion that microgravity-induced synaptic plasticity in medial extrastiola hair cells resulted from the loss of synaptic specializations.

Fig. 8.



[Open in a new tab](#)

Summary box-and-whisker plots of synapse densities (number of synapses per hair cell) in vestibular epithelia from control and microgravity mice. Synapse density per hair cell was lower in the medial extrastiola in microgravity specimens compared with controls (** $P = 0.0027$), whereas comparable measures were similar in the 3 striola regions ($P = 0.85$) and the planar region of the horizontal crista ($P = 0.48$).

In addition to those associated with Shank1a-positive puncta, the total complement of CtBP2-positive puncta also included synaptic ribbons undocked from an active zone, as well as ribbons associated with postsynaptic densities that did not incorporate Shank1a. As indicated above, [Braude et al. \(2015\)](#) found no evidence for postsynaptic densities in the mouse utricular striola that were Shank1a deficient but did not explore other topographic regions. Consequently, we cannot categorically exclude the possibility that some CtBP2-positive puncta were associated with Shank1a-deficient postsynaptic densities. Nonetheless, a comparison of total CtBP2-positive puncta in control and microgravity specimens provided insight regarding whether the change in medial extrastriola synapse density was consistent with a decrease in overall ribbon density in utricular hair cells. This was accomplished by applying the linear mixed-effects analytical model on total CtBP2 puncta densities (puncta per hair cell). These results are shown in [Table 2](#), in which the numerical results from the synapse densities (i.e., CtBP2 and Shank1a associations) are also included. These results ultimately demonstrated that total CtBP2 puncta densities were similar in control and microgravity groups. This finding supports the conclusions that exposure to microgravity does not result in alterations in synaptic ribbon density and that the decrease in synapse density (i.e., paired pre- and postsynaptic markers) was not induced by a decrease in synaptic ribbons in medial extrastriola hair cells. This analysis also provides insight pertinent to reconciliation of the present results with those previously reported by Ross and colleagues ([Ross 1993, 1994, 2000; Ross and Varelas 2005](#)).

Table 2.

Summary distributions of synapse and CtBP2 puncta densities within the topographical regions of control and microgravity utricles ($n = 4$ each)

Parameter	Region	Gravity Condition	N	Percentile					I
				10	25	50	75	90	
Synapse density, count/hair cell	Medial extrastriola	Control	48	6.94	8.19	9.72	12.36	16.02	0.00 ^a
		Microgravity	48	5.04	5.81	6.92	8.37	9.43	0.85
	Striola	Control	70	2.26	2.76	3.61	4.54	5.52	0.48
		Microgravity	68	1.83	2.74	3.77	4.75	5.95	
	Horizontal crista	Control	24	5.88	7.19	9.62	10.86	17.36	0.07 ^a
		Microgravity	24	3.76	5.74	9.01	12.06	13.30	0.08 ^a
	CtBP2 puncta, count/hair cell	Control	48	8.23	10.16	14.80	17.57	22.58	0.99
		Microgravity	48	7.08	8.10	10.74	12.62	15.21	
	Striola	Control	70	4.31	6.50	8.30	9.79	11.69	0.99
		Microgravity	68	6.20	7.52	9.43	11.38	13.48	
	Horizontal crista	Control	24	9.43	10.52	12.52	14.73	19.81	0.99
		Microgravity	24	8.38	9.42	12.83	18.49	21.15	

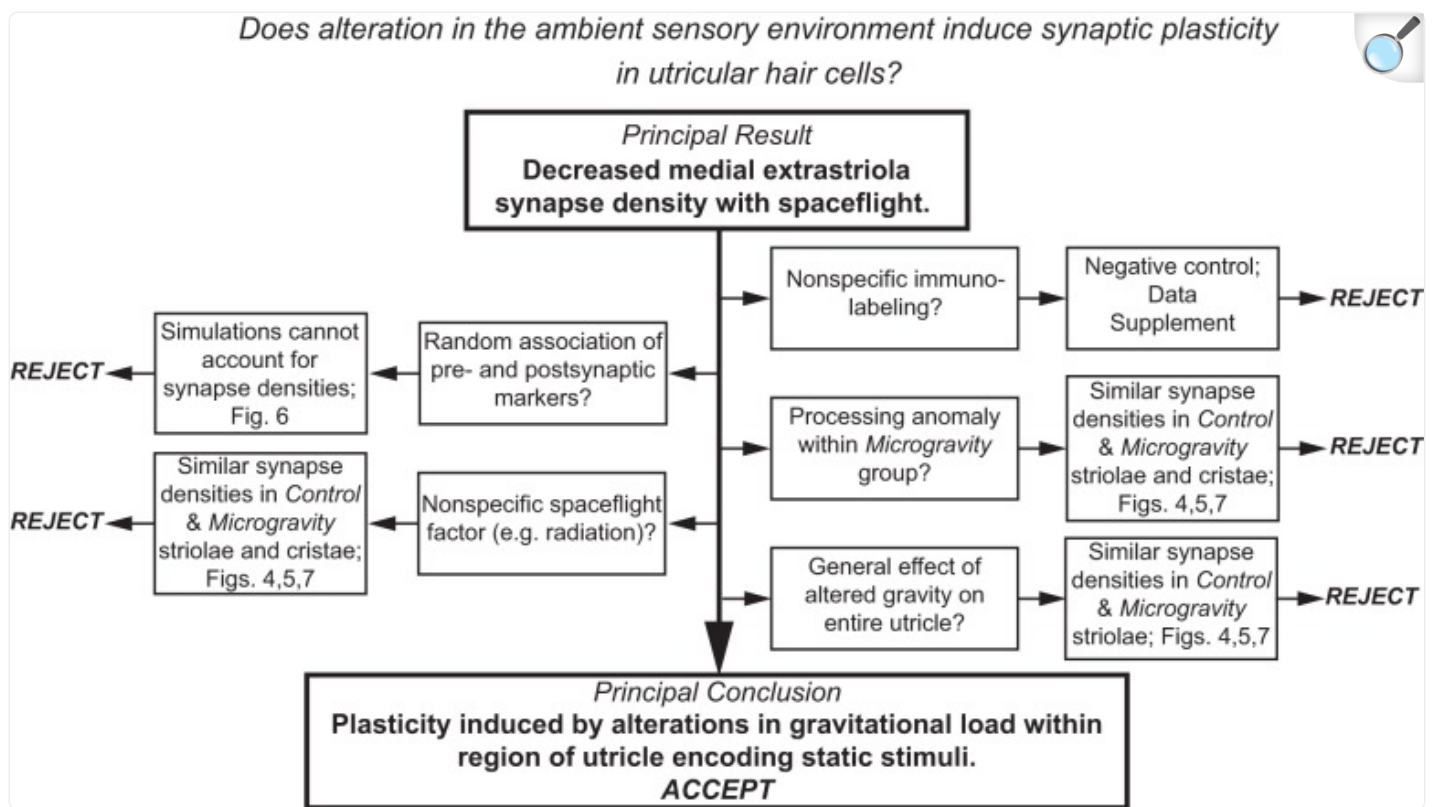
[Open in a new tab](#)

Data are percentiles of synapse and CtBP2 puncta densities within the specified topographical regions of control and microgravity utricles ($n = 4$ each). N value reflects the total number of measurements included in the distribution, including those made by 2 “observers” on the same specimens. Specimens included, in general, 3 subregions from each area (2 for medial extrastriola, 3 from striola, and 1 from the horizontal crista) within the topographical regions specified. As discussed in METHODS, appropriate consideration of nonindependent measures was a critical component of implementation of the linear mixed-effects analytical model.

DISCUSSION

We found that a 2-wk exposure to microgravity induces a reduction in synaptic density in the medial extrastriola of the utricle. The results of this investigation are systematically summarized in Fig. 9, illustrating how the direct outcomes of the various analyses and controls enabled the exclusion of various alternative factors from contributing to the principal result. Because these factors were determined not to be responsible for the decrease in synapse density in the medial extrastriola, we were able to conclude that the synaptic modifications were induced by alteration in the static load acting on the region of the utricle that normally encodes static linear acceleration stimuli.

Fig. 9.



[Open in a new tab](#)

Summary of results elucidating the systematic rejection of potential factors that could contribute to the principal finding of decreased synapse density. The exclusion of these factors leads to the principal conclusion that this decrease represents synaptic plasticity induced by alteration in the ambient gravitational environment associated with spaceflight.

Of course, the design of this investigation included postflight harvesting of temporal bones and specimens of vestibular epithelia, which followed the transition from microgravity to Earth gravity and included periods of hypergravity. As such, we cannot exclude the possibility that the principal finding was affected by changes affected by the transient gravity environment associated with reentry. Evidence to refute this possibility comes from [Ross \(2000\)](#), who showed that the changes in utricular hair cell synapse density were not markedly different in specimens harvested on flight *day 13* and those harvested on postflight *day 0* (and postflight *day 9*, for that matter). The statistical comparisons of this previous study were influenced as much by variability within control specimens (see *Comparisons with Ross's Studies of Spaceflight-Induced Synaptic Plasticity*).

Modifications in Synapse Density Induced by Alterations in the Ambient Gravity Environment

The data and analyses of the present investigation clearly demonstrate that modifications in synapse density were restricted to the utricular medial extrastriola in mice returning from 15 days of spaceflight. This modification amounted to a decrease in synapse density by approximately one-third, whether expressed as synapses per $100 \mu\text{m}^2$ of epithelium or synapses per hair cell. Comparable changes were not found in extensive sampling of the striolae, nor were they found in the horizontal crista planum.

Under normogravitic conditions the utricular epithelium functions under the load imposed by the otolithic membrane, which results in hair cell stereocilia displacement during changes in head orientation with respect to the Earth's gravity vector (e.g., following head tilt). Such changes in head orientation amount to very low frequency, or static, stimuli, and previous investigations of utricular afferent neuron response dynamics have indicated that such low-frequency stimuli modulate the activity of afferent neurons projecting from the extrastriolar regions of the epithelium. Afferents projecting from the striola exhibit phasic (i.e., high pass) dynamic response characteristics ([Fernández and Goldberg 1976b](#); [Goldberg et al. 1990a, 1990b](#)) and are sensitive to the transition component of static head tilts; i.e., their discharge adapts relatively quickly and does not signal the static change in head orientation. The microgravity condition associated with spaceflight results in static unloading of the utricular epithelium, which severely attenuates (or eliminates) the ambient acceleration required for static otolithic membrane displacement concomitant with changes in head orientation. The otolithic membrane retains its mass, and therefore head accelerations due to transient and translational movements remain responsible for otolithic membrane displacement and utricular (and saccular) hair cell stimulation (i.e., head acceleration acting on the otolithic membrane mass leading to the displacing force). Therefore, utricular function persists to encode linear transients and translation head movements under microgravity conditions; only the component of utricular function that depends on ambient gravity (i.e., coding of static head orientation) is compromised.

The localization of the synaptic modifications to the medial extrastriola, and not the striola, provides support to the contention that they were induced by alterations in the ambient gravity environment and not an unforeseen secondary effect of spaceflight. This indicates that the mechanism driving the modification of synapse density was not general to

the utricular epithelium. Of course, we cannot exclude the possibility that alteration in medial extrastriola synapse density resulted from a secondary effect of spaceflight that was restricted to this specific region of utricular topography. We advocate that the compendium of evidence supports the conclusion that the plasticity was the result of alteration in ambient gravitational loading. It remains to be determined whether this synaptic plasticity was driven by cellular mechanisms intrinsic to the epithelium or whether it required central processing and feedback through efferent vestibular neurons.

Our experimental design included analyses of synapse density within the horizontal crista planum as an internal control for factors associated with spaceflight that might induce synaptic changes not directly related to sensory modifications of the utricle. These might include radiation or other environmental stressors ([Berger 2008](#); [Lackner 2014](#); [Reitz et al. 2009](#)). We found synapse density to be unchanged in horizontal crista hair cells, indicating that the modifications in the utricular medial extrastriola were unlikely to have been induced by factors that could more generally mitigate synaptic alterations in vestibular epithelia.

Synapse Density Decrease Implies a “Use It or Lose It” Plasticity Guideline

The unloading of the utricular epithelium in microgravity results in the condition where stereocilia displacements during static changes in head orientation, and the concomitant modulation in hair cell membrane potential, do not occur. This indicates that a fraction of the sensory transduction and signaling cascade, funneled through the presynaptic complexes, does not occur during spaceflight and implies a dramatic reduction in total sensory modulation of the utricular epithelia. The combined evidence, both from the medial extrastriola and from the striola and horizontal crista, suggests that the reduction in synapse density is a result of this diminished total sensory transduction activity and is consistent with a general plasticity guideline where the reduction in sensory activity manifests as a reduction in synapses. This implies that the utricle conforms to a “use it or lose it” plasticity guideline and is consistent with recent findings from an investigation of sensory attenuation in the mammalian cochlea ([Liberman et al. 2015](#)). [Liberman et al. \(2015\)](#) demonstrated a reduction in synapse density within cochlear inner hair cells following removal of the tympanic membrane, representing an experimental treatment to reduce the magnitude of acoustic input. There is some evidence that the retina undergoes similar changes following light deprivation ([Tian and Copenhagen 2001](#)). Therefore, it appears that the general framework of synaptic changes resulting from diminished sensory activity within mechanosensitive hair cells is consistent and may be generalizable to diverse sensory systems, as well. Of course, we cannot exclude the possibility of intrinsic synaptic efficacy changes to the remaining synapses, whereby further alterations in sensory information transmission is mediated through fewer synapses.

In the present study a synapse was defined as the close spatial association of CtBP2 and Shank1a immunolabeling. Our analyses provide additional insight into the subcellular changes underlying the microgravity-induced decrease in these paired associations. The CtBP2-positive ribbons quantified as synapses in the present analyses represented those at the active zone, being in close proximity to the postsynaptic density (PSD) protein Shank1a. Of the remaining complement

of CtBP2-positive ribbons, one component was those undocked, or perhaps “loosely anchored,” to the presynaptic membrane ([Jing et al. 2013](#)). Compromise in the expression of the presynaptic scaffold protein bassoon was shown to increase the incidence of loosely anchored ribbons ([Jing et al. 2013](#)), suggesting that modulation of bassoon expression may represent a potential molecular mechanism to uncouple ribbons from the active zone in response to microgravity exposure. Another potential component of total ribbon density was represented by ribbons at an active zone but not associated with Shank1a-positive PSDs. [Braude et al. \(2015\)](#) showed virtually complete colocalization of Shank1a and PSD immunolabeling in the striolae of mouse utricles, indicating that Shank1a is a constituent of all striolar PSDs. This would seemingly argue against the possibility that a CtBP2-positive ribbon may represent a functional synapse in the absence of association with Shank1a immunolabeling. However, colocalization of PSD and Shank1 immunolabeling in medial extrastriolar afferent dendrites has not been examined, and therefore Shank1a immunolabeling may not identify all medial extrastriolar synapses. Therefore, whereas total CtBP2-positive ribbon density remained stable, the microgravity-induced decrease in synapse density may be explained by either an increase in undocked loosely anchored ribbons or a decrease in the relation of ribbons with Shank1a-positive PSDs.

A third possibility consistent with the present findings is a microgravity-induced decrease in either Shank1a expression or total PSDs in the afferent dendrite. Further investigation into the composition or modification of vestibular afferent PSDs, particularly as they relate to utricular topography, is required to better understand how this crucial component of afferent neurotransmission may be modified.

Comparisons with Ross’ Studies of Spaceflight-Induced Synaptic Plasticity

On the surface, the findings of the present study are not consistent with the previous work of Ross and colleagues, who reported microgravity-induced increases in hair cell synaptic ribbon density ([Ross 1993, 2000](#)). The contrasting findings may be rooted in key differences in experimental models and methodology, which are listed in [Table 3](#). For this discussion, we focused on the results from Neurolab ([Ross 2000](#)), although the salient features are similar to studies conducted during other spaceflight missions ([Ross 1994; Ross and Varelas 2005](#)).

Table 3.Contrasting experimental features between present study and [Ross \(2000\)](#) study

		Present Study	Ross (2000)
Animals			
model	Animal	C57Bl/6J mice	Sprague-Dawley rats
mass†	Age*	16 wk	Unspecified adults
	Sex	Female	Unspecified
	Body mass	20.4	330–404
	Housing	Group	Single
Methodology			
experimental method	Primary	Immunohistochemistry	Transmission electron microscopy
harvest	Specimen	Postflight	In-flight, postflight
	Counting unit	Pre- and postsynaptic pairs, CtBP2+ synaptic ribbons Striola, medial extrastriola	synaptic ribbons “Posterior”‡
Topographic region			
Outcomes	Statistics	Linear mixed model ANOVA with bootstrap resampling	ANOVA
results	Principal	Synapse density decrease (medial extrastriola)	Synaptic ribbon density increase for in-flight harvested specimens
		No change in total CtBP2 ribbon density; striolar ribbon densities nudged upward in microgravity	Variability in controls precluded similar conclusion for postflight day 0 specimens

	Present Study	Ross (2000)
Interpretation	<p>Topography-dependent plasticity associated with dynamic response heterogeneity</p> <p>Synaptic plasticity (density change in pre/postsynaptic components) unlikely to involve change in synaptic ribbon density</p>	<p>Spaceflight-induced ribbon density changes stable to gravity transitions of earth-return</p> <p>Increased ribbon density may not define increase in functional synapses</p>

[Open in a new tab](#)

*Age at landing. †Body mass (g) on day of landing. ‡Descriptions of sampling region are variable in studies by Ross; [Ross \(2000\)](#) specifies their analyses are derived from the posterior region of the rat utricle.

[Table 3](#) highlights a number of differences in the animal subjects between the present study and those used in previous spaceflight experiments ([Ross 2000](#)). Although we do not anticipate major differences in how microgravity-induced utricular hair cell synaptic plasticity is manifested across rodent species, utricles of mice and rats do exhibit remarkable differences in topography (see [Desai et al. 2005](#)), which may affect subtle factors that contribute to plasticity (e.g., otolithic membrane loading and/or unloading). The sex and housing factors may have impacted locomotor behaviors during spaceflight, which may have led to a different repertoire of head movements during flight and differential influencing utricular hair cell synaptic plasticity. Perhaps the largest impact may be borne out of the large difference in body mass between mice and rats, influencing not only locomotor behavior but also other physiological systems (cardiovascular, musculoskeletal) during spaceflight, potentially having notable impact on systemic load sensing that may feed back to the vestibular periphery via efferent mechanisms.

Despite the potential for the aforementioned (and other) factors to be responsible for the apparent contrasting findings of the present investigation and that of [Ross \(2000\)](#), the most likely basis is harbored in the synaptic structure (counting unit) quantified in each investigation. The present study relied on close association between pre- and postsynaptic markers to identify a synapse, but we also quantified all CtBP2-positive puncta, including those not paired with postsynaptic Shank1a immunolabeling. We found that total CtBP2-positive puncta densities (paired plus unpaired) were similar within both striolar and medial extrastriolar regions of control and microgravity utricles. Although [Ross \(2000\)](#) applied strict criteria to define a synaptic ribbon (i.e., electron-opaque structure surrounded by a halo of vesicles), every ribbon was counted, including those that were completely within the hair cell cytoplasm (i.e., not apposed to the presynaptic membrane). Furthermore, it appears that multiple ribbons in a cluster were counted individually rather than as one synaptic complex. In the present investigation, intracytoplasmic (i.e., “undocked”) CtBP2-positive puncta would have contributed to the total count, but not in the synapse counts. Furthermore, CtBP2 immunolabeling does not enable

counting of closely situated, or clustered, ribbons. Quantification of CtBP2-positive puncta over large regions of utricular epithelia provides a much broader perspective than can be achieved through spatially constricted ultrastructural analyses. Therefore, there appears to be a number of experimental differences that could belie the apparent contrasting findings between the present and previous ([Ross 2000](#)) studies.

What are the Drivers of Utricular Hair Cell Synaptic Plasticity?

A compelling question stemming directly from the present results concerns the intra- and/or intercellular signals driving the modifications in synapse density. Two scenarios seem most plausible to account for how changes in utricular loading may lead to alterations in pathways responsible for establishment of afferent synapses. One possibility is that the principal driver of plasticity requires a signal generated through sensory integration within the central nervous system and transmitted centrifugally by vestibular efferent neurons. Of course, the cellular mechanisms through which an efferent signal might drive synaptic modifications within hair cells and afferent neurons are unknown. Efferent projections are primarily cholinergic, acting through nicotinic ([Holt et al. 2015; Jordan et al. 2013](#)) and muscarinic receptors ([Holt et al. 2017; Zhou et al. 2013](#)) on type II hair cells and afferent processes (i.e., calyces, boutons, and dendritic branches ([Jordan et al. 2015; Lysakowski and Goldberg 1997; Pujol et al. 2014](#))). Any efferent-mediated plasticity in type I hair cells would require an indirect mechanism involving the afferent calyx (e.g., altering the postsynaptic receptor complex). Whereas nicotinic receptor activation contributes to a broad array of neurotransmission modulatory effects in the central nervous system, none of these have been shown to be mediated through inner ear-specific $\alpha 9$ or $\alpha 10$ receptors ([Dajas-Bailador and Wonnacott 2004](#)). [Morley et al. \(2017\)](#) recently showed that vestibular evoked potential thresholds were elevated in $\alpha 9$ and $\alpha 10$ knockout mice, suggesting that chronic deprivation of a predominant form of efferent input to the vestibular epithelia manifest in sensitivity changes that may be similar to diminished synapse density.

The second possibility is that the pathways for synaptic modifications are intrinsic to the hair cell. Such a mechanism would likely be “promiscuous” in affecting both type I and II hair cells. Of course, both intrinsic and efferent-mediated mechanisms might be involved, perhaps resulting in aspects of each mechanism segregating to distinct hair cell types.

Could an efferent mechanism differentially drive plasticity in different topographic regions? This would seemingly require differential projections of individual efferent neurons to the striola and medial extrastriola. Although we previously found similarities in the densities of cholinergic terminals in these two utricular regions ([Sultemeier et al. 2010](#)), we know of no direct evidence in mouse utricle demonstrating topography-dependent projection loci of efferent neurons. Evidence does exist, however, for such an organization in efferent projections to crista neuroepithelia ([Purcell and Perachio 1997](#)), supporting the plausibility of this mechanism at the circuit level.

It should be noted that although the present study did not distinguish synapse counts by hair cell types, there are type I and II hair cells in all regions of epithelia examined. Therefore, it is unlikely that our findings can be explained, for

example, by the lack of plasticity in type I hair cells in the case that the driver is efferent mediated. The difference in the fraction of type II hair cells estimated in the striola and extrastriola (40% and 50%, respectively; Desai et al. 2005) makes it unlikely that synaptic plasticity in the striola went undetected even if plasticity were restricted to type II hair cells.

Evidence of Peripheral Vestibular Adaptation in Astronauts

The present investigation demonstrates that 15 days of microgravity exposure, which was a typical mission duration of the space shuttle era, is sufficient to induce structural plasticity in utricular hair cell afferent synapses in the mouse and that this change persists in the immediate postlanding hours. However, direct evidence of changes in the peripheral vestibular neuroepithelia of astronauts resulting from microgravity exposures of spaceflight has been inconclusive. In one of the more recent investigations, ocular counterrolling (OCR) was recorded from 7 astronauts at R+0 (within 2–24 h after landing), R+2 days, and R+4 days following space shuttle missions lasting 10–13 days ([Clément et al. 2007](#)). OCR represents a direct response of the utricle to tilt-induced (i.e., low frequency) shear of the otolithic membrane and likely represents a test of utricular extrastriola regions. This examination revealed no difference in this subject group in any of the postflight tests compared with preflight studies. However, these investigators acknowledged the lack of sufficient power that hampered previous investigations with similar experimental goals and implemented methods to reduce OCR variability. At the same time, the same cohort of astronauts exhibited differences in the perception of roll tilt during early postflight tests compared with preflight. This does not necessarily conflict with the OCR findings suggesting the absence of spaceflight-induced changes in utricular neuroepithelia in astronauts, only that the OCR changes in this subject cohort may be very small in the context of response variance and subject number.

There is recent evidence, however, demonstrating that longer spaceflight exposures incumbent with a 6-mo sojourn aboard the International Space Station do result in diminished vestibular function. [Hallgren et al. \(2016\)](#) have shown that OCR recorded from 25 astronauts/cosmonauts during the immediate postlanding period after each of their missions was attenuated by an average of 30%. Although the periods of microgravity exposure experienced by these subjects were vastly different from that experienced by mice in the present investigation, the outcome was suggestively congruent with the synapse density changes we report here. Although direct causal correlations are premature, the similarities suggest that the microgravity effects are relatively rapid and asymptotic, and do not progress with spaceflight duration.

Translational Impact of Vestibular Hair Cell Synaptic Plasticity

The principal finding of the present study indicates that mature vestibular hair cells retain capabilities for structural plasticity manifested through modulation of synapse density. Investigations are ongoing that are testing the hypothesis that synapse density increases may result from exposure to centrifugation-induced hypergravity, which would provide

the foundation for future research into the molecular mechanisms through which these modifications are induced. This research will provide insight and strategies for inner ear rehabilitation through the induction of synapse density increases in conditions of vestibular paresis.

GRANTS

This work was supported by NASA Grant NNX09AL57G.

DISCLOSURES

No conflicts of interest, financial or otherwise, are declared by the authors.

AUTHOR CONTRIBUTIONS

D.R.S. and L.F.H. performed experiments; D.R.S., K.R.C., and L.F.H. analyzed data; D.R.S., F.E.S., and L.F.H. interpreted results of experiments; D.R.S. and L.F.H. prepared figures; D.R.S. and L.F.H. drafted manuscript; D.R.S., F.E.S., and L.F.H. edited and revised manuscript; D.R.S., K.R.C., F.E.S., and L.F.H. approved final version of manuscript; F.E.S. and L.F.H. conceived and designed research.

ACKNOWLEDGMENTS

We gratefully acknowledge the dedicated assistance of a small team of outstanding undergraduates that conducted the image analyses of immunohistochemically labeled utricular and crista epithelia. Members of Team Synapse included Daniel Brenners, Daniel Chang, Amie Chen, and Charles Hu. The contributions of Dr. Patricia Quiñones during early stages of this work are acknowledged. Specimens from the Y16 mouse line were provided by Dr. D. Simmons. We also acknowledge the insightful recommendations of Dr. N. Wisniewski on implementation of the linear mixed-effects models used in our statistical analyses. In addition, we are indebted to Dr. Richard Boyle, Paula Dumars, and Vera Vizir for their phenomenal support (programmatic and technical) of NASA's Biospecimen Sharing Program, of which this project was a component. Finally, the collegiality among all Biospecimen Sharing Program investigators and associates contributed in no small way to the success of this scientific spaceflight mission.

Specimens were harvested at the Kennedy Space Center.

Present address of D. R. Sultemeier: Biology Department, University of Puget Sound; 1500 N. Warner St., CMB 1088, Tacoma, WA 98416.

REFERENCES

1. Bailey JF, Hargens AR, Cheng KK, Lotz JC. Effect of microgravity on the biomechanical properties of lumbar and caudal intervertebral discs in mice. *J Biomech* 47: 2983–2988, 2014. doi: 10.1016/j.jbiomech.2014.07.005. [[DOI](#)] [[PubMed](#)] [[Google Scholar](#)]
2. Bates D, Mächler M, Bolker BM, Walker SC. Fitting linear mixed-effects models using lme4. *J Stat Softw* 67: 1–48, 2015. doi: 10.18637/jss.v067.i01. [[DOI](#)] [[Google Scholar](#)]
3. Behnke BJ, Stabley JN, McCullough DJ, Davis RT 3rd, Dominguez JM 2nd, Muller-Delp JM, Delp MD. Effects of spaceflight and ground recovery on mesenteric artery and vein constrictor properties in mice. *FASEB J* 27: 399–409, 2013. doi: 10.1096/fj.12-218503. [[DOI](#)] [[PMC free article](#)] [[PubMed](#)] [[Google Scholar](#)]
4. Berger T. Radiation dosimetry onboard the International Space Station ISS. *Z Med Phys* 18: 265–275, 2008. doi: 10.1016/j.zemedi.2008.06.014. [[DOI](#)] [[PubMed](#)] [[Google Scholar](#)]
5. Blaber EA, Dvorochkin N, Lee C, Alwood JS, Yousuf R, Pianetta P, Globus RK, Burns BP, Almeida EA. Microgravity induces pelvic bone loss through osteoclastic activity, osteocytic osteolysis, and osteoblastic cell cycle inhibition by CDKN1a/p21. *PLoS One* 8: e61372, 2013. doi: 10.1371/journal.pone.0061372. [[DOI](#)] [[PMC free article](#)] [[PubMed](#)] [[Google Scholar](#)]
6. Braude JP, Vijayakumar S, Baumgartner K, Laurine R, Jones TA, Jones SM, Pyott SJ. Deletion of Shank1 has minimal effects on the molecular composition and function of glutamatergic afferent postsynapses in the mouse inner ear. *Hear Res* 321: 52–64, 2015. doi: 10.1016/j.heares.2015.01.008. [[DOI](#)] [[PMC free article](#)] [[PubMed](#)] [[Google Scholar](#)]
7. Chang TT, Spurlock SM, Candelario TL, Grenon SM, Hughes-Fulford M. Spaceflight impairs antigen-specific tolerance induction in vivo and increases inflammatory cytokines. *FASEB J* 29: 4122–4132, 2015. doi: 10.1096/fj.15-275073. [[DOI](#)] [[PMC free article](#)] [[PubMed](#)] [[Google Scholar](#)]
8. Clément G, Denise P, Reschke MF, Wood SJ. Human ocular counter-rolling and roll tilt perception during off-vertical axis rotation after spaceflight. *J Vestib Res* 17: 209–215, 2007. [[PubMed](#)] [[Google Scholar](#)]
9. Dajas-Bailador F, Wonnacott S. Nicotinic acetylcholine receptors and the regulation of neuronal signalling. *Trends Pharmacol Sci* 25: 317–324, 2004. doi: 10.1016/j.tips.2004.04.006. [[DOI](#)] [[PubMed](#)] [[Google Scholar](#)]
10. Desai SS, Zeh C, Lysakowski A. Comparative morphology of rodent vestibular periphery. I. Saccular and utricular maculae. *J Neurophysiol* 93: 251–266, 2005. doi: 10.1152/jn.00746.2003. [[DOI](#)] [[PubMed](#)]

[[Google Scholar](#)]

11. Dulan D, Safieddine S, Jones SM, Petit C. Otoferlin is critical for a highly sensitive and linear calcium-dependent exocytosis at vestibular hair cell ribbon synapses. *J Neurosci* 29: 10474–10487, 2009. doi: 10.1523/JNEUROSCI.1009-09.2009. [[DOI](#)] [[PMC free article](#)] [[PubMed](#)] [[Google Scholar](#)]
12. Eatock RA, Songer JE. Vestibular hair cells and afferents: two channels for head motion signals. *Annu Rev Neurosci* 34: 501–534, 2011. doi: 10.1146/annurev-neuro-061010-113710. [[DOI](#)] [[PubMed](#)] [[Google Scholar](#)]
13. Feng G, Mellor RH, Bernstein M, Keller-Peck C, Nguyen QT, Wallace M, Nerbonne JM, Lichtman JW, Sanes JR. Imaging neuronal subsets in transgenic mice expressing multiple spectral variants of GFP. *Neuron* 28: 41–51, 2000. doi: 10.1016/S0896-6273(00)00084-2. [[DOI](#)] [[PubMed](#)] [[Google Scholar](#)]
14. Fernández C, Goldberg JM. Physiology of peripheral neurons innervating otolith organs of the squirrel monkey. I. Response to static tilts and to long-duration centrifugal force. *J Neurophysiol* 39: 970–984, 1976a. [[DOI](#)] [[PubMed](#)] [[Google Scholar](#)]
15. Fernández C, Goldberg JM. Physiology of peripheral neurons innervating otolith organs of the squirrel monkey. III. Response dynamics. *J Neurophysiol* 39: 996–1008, 1976b. [[DOI](#)] [[PubMed](#)] [[Google Scholar](#)]
16. Goldberg JM, Desmadryl G, Baird RA, Fernández C. The vestibular nerve of the chinchilla. IV. Discharge properties of utricular afferents. *J Neurophysiol* 63: 781–790, 1990a. [[DOI](#)] [[PubMed](#)] [[Google Scholar](#)]
17. Goldberg JM, Desmadryl G, Baird RA, Fernández C. The vestibular nerve of the chinchilla. V. Relation between afferent discharge properties and peripheral innervation patterns in the utricular macula. *J Neurophysiol* 63: 791–804, 1990b. [[DOI](#)] [[PubMed](#)] [[Google Scholar](#)]
18. Gundersen HJ. Notes on estimation of numerical density of arbitrary profiles: the edge effect. *J Microsc* 111: 219–223, 1977. doi: 10.1111/j.1365-2818.1977.tb00062.x. [[DOI](#)] [[Google Scholar](#)]
19. Hallgren E, Kornilova L, Fransen E, Glukhikh D, Moore ST, Clément G, Van Ombergen A, MacDougall H, Naumov I, Wuyts FL. Decreased otolith-mediated vestibular response in 25 astronauts induced by long-duration spaceflight. *J Neurophysiol* 115: 3045–3051, 2016. doi: 10.1152/jn.00065.2016. [[DOI](#)] [[PMC free article](#)] [[PubMed](#)] [[Google Scholar](#)]
20. Holt JC, Jordan PM, Lysakowski A, Shah A, Barsz K, Contini D. Muscarinic acetylcholine receptors and M-currents underlie efferent-mediated slow excitation in calyx-bearing vestibular afferents. *J Neurosci* 37: 1873–1887, 2017. doi: 10.1523/JNEUROSCI.2322-16.2017. [[DOI](#)] [[PMC free article](#)] [[PubMed](#)] [[Google Scholar](#)]

21. Holt JC, Kewin K, Jordan PM, Cameron P, Klapczynski M, McIntosh JM, Crooks PA, Dwoskin LP, Lysakowski A. Pharmacologically distinct nicotinic acetylcholine receptors drive efferent-mediated excitation in calyx-bearing vestibular afferents. *J Neurosci* 35: 3625–3643, 2015. doi: 10.1523/JNEUROSCI.3388-14.2015. [[DOI](#)] [[PMC free article](#)] [[PubMed](#)] [[Google Scholar](#)]]
22. Huang LC, Barclay M, Lee K, Peter S, Housley GD, Thorne PR, Montgomery JM. Synaptic profiles during neurite extension, refinement and retraction in the developing cochlea. *Neural Dev* 7: 38, 2012. doi: 10.1186/1749-8104-7-38. [[DOI](#)] [[PMC free article](#)] [[PubMed](#)] [[Google Scholar](#)]]
23. Jing Z, Rutherford MA, Takago H, Frank T, Fejtova A, Khimich D, Moser T, Strenzke N. Disruption of the presynaptic cytomatrix protein bassoon degrades ribbon anchorage, multiquantal release, and sound encoding at the hair cell afferent synapse. *J Neurosci* 33: 4456–4467, 2013. doi: 10.1523/JNEUROSCI.3491-12.2013. [[DOI](#)] [[PMC free article](#)] [[PubMed](#)] [[Google Scholar](#)]]
24. Jordan PM, Fettis M, Holt JC. Efferent innervation of turtle semicircular canal cristae: comparisons with bird and mouse. *J Comp Neurol* 523: 1258–1280, 2015. doi: 10.1002/cne.23738. [[DOI](#)] [[PMC free article](#)] [[PubMed](#)] [[Google Scholar](#)]]
25. Jordan PM, Parks XX, Contini D, Holt JC. A review of synaptic mechanisms of vestibular efferent signaling in turtles: extrapolation to efferent actions in mammals. *J Vestib Res* 23: 161–175, 2013. doi: 10.3233/VES-130492. [[DOI](#)] [[PubMed](#)] [[Google Scholar](#)]]
26. Lackner JR. Motion sickness: more than nausea and vomiting. *Exp Brain Res* 232: 2493–2510, 2014. doi: 10.1007/s00221-014-4008-8. [[DOI](#)] [[PMC free article](#)] [[PubMed](#)] [[Google Scholar](#)]]
27. Li A, Xue J, Peterson EH. Architecture of the mouse utricle: macular organization and hair bundle heights. *J Neurophysiol* 99: 718–733, 2008. doi: 10.1152/jn.00831.2007. [[DOI](#)] [[PubMed](#)] [[Google Scholar](#)]]
28. Liberman MC, Liberman LD, Maison SF. Chronic conductive hearing loss leads to cochlear degeneration. *PLoS One* 10: e0142341, 2015. doi: 10.1371/journal.pone.0142341. [[DOI](#)] [[PMC free article](#)] [[PubMed](#)] [[Google Scholar](#)]]
29. Lysakowski A, Gaboyard-Niay S, Calin-Jageman I, Chatlani S, Price SD, Eatock RA. Molecular microdomains in a sensory terminal, the vestibular calyx ending. *J Neurosci* 31: 10101–10114, 2011. doi: 10.1523/JNEUROSCI.0521-11.2011. [[DOI](#)] [[PMC free article](#)] [[PubMed](#)] [[Google Scholar](#)]]
30. Lysakowski A, Goldberg JM. A regional ultrastructural analysis of the cellular and synaptic architecture in the chinchilla cristae ampullares. *J Comp Neurol* 389: 419–443, 1997. doi: [a href="#">DOI] [[PMC free article](#)] [[PubMed](#)] [[Google Scholar](#)]]

31. Mayhew TM. How to count synapses unbiasedly and efficiently at the ultrastructural level: proposal for a standard sampling and counting protocol. *J Neurocytol* 25: 793–804, 1996. doi: 10.1007/BF02284842. [DOI] [PubMed] [Google Scholar]
32. Mednieks M, Khatri A, Rubenstein R, Burleson JA, Hand AR. Microgravity alters the expression of salivary proteins. *Oral Health Dent Manag* 13: 211–216, 2014. [PubMed] [Google Scholar]
33. Meredith FL, Rennie KJ. Zonal variations in K^+ currents in vestibular crista calyx terminals. *J Neurophysiol* 113: 264–276, 2015. doi: 10.1152/jn.00399.2014. [DOI] [PMC free article] [PubMed] [Google Scholar]
34. Morley BJ, Lysakowski A, Vijayakumar S, Menapace D, Jones TA. Nicotinic acetylcholine receptors regulate vestibular afferent gain and activation timing. *J Comp Neurol* 525: 1216–1233, 2017. doi: 10.1002/cne.24131. [DOI] [PMC free article] [PubMed] [Google Scholar]
35. Pujol R, Pickett SB, Nguyen TB, Stone JS. Large basolateral processes on type II hair cells are novel processing units in mammalian vestibular organs. *J Comp Neurol* 522: 3141–3159, 2014. doi: 10.1002/cne.23625. [DOI] [PMC free article] [PubMed] [Google Scholar]
36. Purcell IM, Perachio AA. Three-dimensional analysis of vestibular efferent neurons innervating semicircular canals of the gerbil. *J Neurophysiol* 78: 3234–3248, 1997. [DOI] [PubMed] [Google Scholar]
37. R Development Core Team R: A language and Environment for Statistical Computing. Vienna, Austria: R Foundation for Statistical Computing, 2012. [Google Scholar]
38. Reitz G, Berger T, Bilski P, Facius R, Hajek M, Petrov V, Puchalska M, Zhou D, Bossler J, Akatov Y, Shurshakov V, Olko P, Ptaszkiewicz M, Bergmann R, Fugger M, Vana N, Beaujean R, Burmeister S, Bartlett D, Hager L, Pálfalvi J, Szabó J, O’Sullivan D, Kitamura H, Uchihori Y, Yasuda N, Nagamatsu A, Tawara H, Benton E, Gaza R, McKeever S, Sawakuchi G, Yukihara E, Cucinotta F, Semones E, Zapp N, Miller J, Dettmann J. Astronaut’s organ doses inferred from measurements in a human phantom outside the international space station. *Radiat Res* 171: 225–235, 2009. doi: 10.1667/RR1559.1. [DOI] [PubMed] [Google Scholar]
39. Ross MD. Morphological changes in rat vestibular system following weightlessness. *J Vestib Res* 3: 241–251, 1993. [PubMed] [Google Scholar]
40. Ross MD. A spaceflight study of synaptic plasticity in adult rat vestibular maculas. *Acta Otolaryngol Suppl* 516: 1–14, 1994. [PubMed] [Google Scholar]
41. Ross MD. Changes in ribbon synapses and rough endoplasmic reticulum of rat utricular macular hair cells

in weightlessness. *Acta Otolaryngol* 120: 490–499, 2000. doi: 10.1080/000164800750045983. [DOI] [PubMed] [Google Scholar]

42. Ross MD, Varelas J. Synaptic ribbon plasticity, ribbon size and potential regulatory mechanisms in utricular and saccular maculae. *J Vestib Res* 15: 17–30, 2005. [PubMed] [Google Scholar]

43. Rüsch A, Lysakowski A, Eatock RA. Postnatal development of type I and type II hair cells in the mouse utricle: acquisition of voltage-gated conductances and differentiated morphology. *J Neurosci* 18: 7487–7501, 1998. [DOI] [PMC free article] [PubMed] [Google Scholar]

44. Sadeghi SG, Pyott SJ, Yu Z, Glowatzki E. Glutamatergic signaling at the vestibular hair cell calyx synapse. *J Neurosci* 34: 14536–14550, 2014. doi: 10.1523/JNEUROSCI.0369-13.2014. [DOI] [PMC free article] [PubMed] [Google Scholar]

45. Schmitz F, Königstorfer A, Südhof TC. RIBEYE, a component of synaptic ribbons: a protein's journey through evolution provides insight into synaptic ribbon function. *Neuron* 28: 857–872, 2000. doi: 10.1016/S0896-6273(00)00159-8. [DOI] [PubMed] [Google Scholar]

46. Schweizer FE, Savin D, Luu C, Sultemeier DR, Hoffman LF. Distribution of high-conductance calcium-activated potassium channels in rat vestibular epithelia. *J Comp Neurol* 517: 134–145, 2009. doi: 10.1002/cne.22148. [DOI] [PMC free article] [PubMed] [Google Scholar]

47. Stabley JN, Dominguez JM 2nd, Dominguez CE, Mora Solis FR, Ahlgren J, Behnke BJ, Muller-Delp JM, Delp MD. Spaceflight reduces vasoconstrictor responsiveness of skeletal muscle resistance arteries in mice. *J Appl Physiol* (1985) 113: 1439–1445, 2012. doi: 10.1152/japplphysiol.00772.2012. [DOI] [PubMed] [Google Scholar]

48. Stella SL Jr, Vila A, Hung AY, Rome ME, Huynh U, Sheng M, Kreienkamp HJ, Brecha NC. Association of shank 1A scaffolding protein with cone photoreceptor terminals in the mammalian retina. *PLoS One* 7: e43463, 2012. doi: 10.1371/journal.pone.0043463. [DOI] [PMC free article] [PubMed] [Google Scholar]

49. Sultemeier DR, Soteropoulos C, Simmons DD, Hoffman LF. Distribution of efferent terminals in adult mouse vestibular neuroepithelia. *Abstr Midwinter Res Meet Assoc Res Otolaryngol* 33: 323, 2010. [Google Scholar]

50. Tian N, Copenhagen DR. Visual deprivation alters development of synaptic function in inner retina after eye opening. *Neuron* 32: 439–449, 2001. doi: 10.1016/S0896-6273(01)00470-6. [DOI] [PubMed] [Google Scholar]

51. Zhou T, Wang Y, Guo CK, Zhang WJ, Yu H, Zhang K, Kong WJ. Two distinct channels mediated by m2mAChR and α9nAChR co-exist in type II vestibular hair cells of guinea pig. *Int J Mol Sci* 14: 8818–8831,

Articles from Journal of Neurophysiology are provided here courtesy of **American Physiological Society**